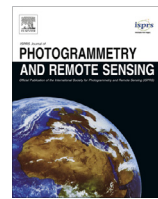




Contents lists available at ScienceDirect

## ISPRS Journal of Photogrammetry and Remote Sensing

journal homepage: [www.elsevier.com/locate/isprsjprs](http://www.elsevier.com/locate/isprsjprs)

# A new deep convolutional neural network for fast hyperspectral image classification

M.E. Paoletti\*, J.M. Haut, J. Plaza, A. Plaza

Hyperspectral Computing Laboratory (HyperComp), Department of Computer Technology and Communications, Escuela Politecnica de Caceres, University of Extremadura, Avenida de la Universidad s/n, E-10002 Caceres, Spain

## ARTICLE INFO

## Article history:

Received 31 May 2017

Received in revised form 27 October 2017

Accepted 29 November 2017

Available online xxxx

## Keywords:

Hyperspectral imaging

Deep learning

Convolutional neural networks (CNNs)

Classification

Graphics processing units (GPUs)

## ABSTRACT

Artificial neural networks (ANNs) have been widely used for the analysis of remotely sensed imagery. In particular, convolutional neural networks (CNNs) are gaining more and more attention in this field. CNNs have proved to be very effective in areas such as image recognition and classification, especially for the classification of large sets composed by two-dimensional images. However, their application to multispectral and hyperspectral images faces some challenges, especially related to the processing of the high-dimensional information contained in multidimensional data cubes. This results in a significant increase in computation time. In this paper, we present a new CNN architecture for the classification of hyperspectral images. The proposed CNN is a 3-D network that uses both spectral and spatial information. It also implements a border mirroring strategy to effectively process border areas in the image, and has been efficiently implemented using graphics processing units (GPUs). Our experimental results indicate that the proposed network performs accurately and efficiently, achieving a reduction of the computation time and increasing the accuracy in the classification of hyperspectral images when compared to other traditional ANN techniques.

© 2017 International Society for Photogrammetry and Remote Sensing, Inc. (ISPRS). Published by Elsevier B.V. All rights reserved.

## 1. Introduction

Remote sensing image acquisition and processing has become very important in recent times in Earth observation problems, exhibiting many practical applications such as monitoring and management of the environment, agriculture or security and defense/intelligence issues. Of particular importance is the computationally efficient processing of images formed by multiple spectral bands, called multispectral and hyperspectral images. These kinds of images collect information corresponding to large observation areas on the surface of the Earth, using dozens/hundreds of contiguous spectral bands (Chang, 2003), thus creating a three-dimensional data cube with size significantly larger than traditional remotely sensed images. As a result, multispectral and hyperspectral images require particular computational improvements, especially for their storage and advanced processing.

Several methods have been developed for fast processing and classification of multispectral and hyperspectral images (Cheng et al., 2017; Yuan et al., 2015), from those that only use spatial or spectral information to those that combine both kinds of data. This includes unsupervised techniques such as clustering (Haut et al.,

2017a; Tarabalka et al., 2009; Paoletti et al., 2017). However, supervised classifiers are often preferred, due to their capacity to provide high classification accuracies, although these methods may be affected by the limited availability of training samples as they generally need a large number of samples in order to obtain those good results. In particular, supervised methods face challenges in the classification of hyperspectral images due to the unbalance between the high dimensionality of the data and the limited number of training samples available in practice (*Hughes phenomenon*) (Khodadadzadeh et al., 2014). In this sense, support vector machines (SVMs) (Scholkopf and Smola, 2001) and multinomial logistic regression (MLR) (Böhning, 1992) have been proved to be very useful for the supervised classification of hyperspectral images due to their ability to deal with large input spaces (Melgani and Bruzzone, 2004; Fauvel et al., 2008; Plaza et al., 2009; Camps-Valls and Bruzzone, 2005; Wu et al., 2015; Haut et al., 2017b). Also, some sampling query strategies have been proposed to address the limited availability of training samples, such as semi-supervised and active learning methods (Li et al., 2010, 2011; Rajan et al., 2008).

At this point, we can highlight several spatial-spectral classification methods that combine the strengths of semi-supervised methods and active learning techniques, for example those based on morphological component analysis (MCA) (Starck et al., 2005), a method that decomposes images into texture and cartoon

\* Corresponding author.

E-mail address: [mpaoletti@alumnos.unex.es](mailto:mpaoletti@alumnos.unex.es) (M.E. Paoletti).

(piecewise smooth) parts. In Zhou and Prasad (2017), authors presented a new framework that combines active and semi-supervised learning with MCA for hyperspectral image classification. Also, in Xu et al. (2016b) authors presented a new classification framework for the fusion of hyperspectral and light detection and ranging (LiDAR) data, combining MCA for textural feature extraction and MLR for classification purposes. The multiple MCA (MMCA) (Xu et al., 2016a) is an extension of the MCA that uses both spatial and spectral features. Its goal is to separate an image into two components: a smoothness component and a texture component.

On the other hand, due to their success in the field of pattern recognition (Bishop, 1995; Atkinson and Tatnall, 1997) and the availability of multiple training techniques (including machine learning, deep learning and active learning techniques, as well as supervised, unsupervised and semi-supervised approaches) to deal with linearly non-separable data (Benediktsson and Swain, 1990), artificial neural networks (ANNs) have attracted the attention of a large number of researchers in the area of hyperspectral image classification and analysis (Benediktsson et al., 1993; Yang, 1999) as compared to probabilistic methods. In particular, we highlight the use of convolutional neural networks (CNNs) (LeCun et al., 1998a) as a powerful deep learning model for image classification, which can effectively combine the spatial and spectral information.

### 1.1. Deep learning and CNNs: a review

For years, building a machine learning system required a great deal of effort in designing a feature extractor that would transform raw data (i.e. pixel values from an image) into a feature vector from which the learning subsystem could detect/classify patterns (LeCun et al., 2015). Deep learning (or deep structured learning) emerged in 2006 with deep belief networks (DBNs)<sup>1</sup> (Hinton et al., 2006; Hinton and Salakhutdinov, 2006) as a part of a machine learning system that exploits many layers of non-linear information processing for supervised or unsupervised feature extraction and transformation, and also for pattern analysis and classification (Bengio, 2009).

After DBNs, two new unsupervised deep models were developed: (1) a method for learning sparse, overcomplete features that uses a linear encoder-decoder preceded by a sparsifying non-linearity that turns a code vector into a quasi-binary sparse code vector (Ranzato et al., 2006) and (2) a variant of autoencoder with greedy layer-wise training (Bengio et al., 2007).

With the advancement of technology (both hardware and software) and the development of new optimization algorithms<sup>2</sup> (LeCun et al., 1998b) new milestones were achieved in deep learning, giving as result three types of deep methods:

- Unsupervised deep networks (generative learning): these methods work without labeled classes, looking for patterns between pixels through capturing high-order correlation of data (e.g. autoencoder-based methods<sup>3</sup> (Licciardi and Del Frate, 2011;

<sup>1</sup> A DBN is composed by a stack of restricted Boltzmann machines (Smolensky, 1986; Larochelle and Bengio, 2008) (RBMs). The DBN core is a greedy learning algorithm that optimizes the network weights layer by layer. Its complexity grows linearly with the size and depth of the network.

<sup>2</sup> For example, new variants of gradient descent optimizer were developed, including batch and mini-batch gradient descent, the stochastic gradient descent (SGD) or the included momentum in SGD (Qian, 1999). New optimizers also appear as Adagrad optimizer (Duchi et al., 2011) and its extension Adadelta (Zeiler, 2012) or the Adam optimizer (Kingma and Ba, 2014).

<sup>3</sup> An autoencoder (Cho, 2014; Karhunen et al., 2015) is a neural network (or mapping method) where the desired output is equal to the input data vector. We can distinguish between linear autoencoders, with only one hidden layer that works like a principal component analysis (PCA) if its weights between the encoder and decoder are tied, and non-linear or deep autoencoders, which have more modeling power by employing multiple nonlinear intermediate layers symmetrically in the encoder and decoder (Cho, 2014).

Chen et al., 2014), RBMs (Midhun et al., 2014), DBNs (Li et al., 2014b), and deep Boltzmann machines or DBMs (Salakhutdinov and Hinton, 2009; Wu et al., 2016)).

- Supervised deep networks (discriminative deep networks): these models work with labeled information and their goal is to categorize the input data in these labels. They represent the most common form of machine learning, deep or not (LeCun et al., 2015), and these kinds of models are usually more efficient to train and test, more flexible to construct, and more suitable for end-to-end learning of complex systems (Deng and Yu, 2014). We can distinguish between linear supervised deep method<sup>4</sup> (e.g. deep neural networks or DNNs<sup>5</sup> with linear activation functions) and non-linear supervised methods (e.g. deep stacking networks or DSNs (He et al., 2016), recurrent neural networks or RNNs<sup>6</sup> and Convolutional neural networks or CNNs (LeCun et al., 2015)).<sup>7</sup>
- Hybrid deep networks (semisupervised methods): these methods make use of both generative and discriminative model components, i.e., they work with and without labeled data (e.g. generative adversarial networks or GANs (Goodfellow et al., 2014)). Semi-supervised learning is very useful in hyperspectral image classification in order to deal with the limited training samples problem (Ma et al., 2016).

Focusing on CNNs, these supervised non-linear models are a special type of deep learning model that is inspired by neuroscience (Ghamisi et al., 2017) and are designed to process data that come in the form of multiple arrays. The literature on CNN applied to remote sensing classification shows different points of view in the way these models are used. Basically there are three ways to apply CNNs:

1. Extracting only spectral information: spectral-based classification approaches are conceptually simple and easy to be implemented, but they neglect the spatial components (Li et al., 2014a). Normally, these methods assume that each pixel is pure and typically labeled as a single land use and land cover type (Fisher, 1997). For spectral feature classification with CNNs, the spectral feature of the original image data is directly deployed as the input vector (Zhang et al., 2016a), so we obtain a 1-D CNN architecture that receives  $N \times 1$  input vectors, where  $N$  is the number of spectral bands (Ghamisi et al., 2017; Hu et al., 2015b; Chen et al., 2016).
2. Extracting only spatial information: these models consider the neighboring pixels of a certain pixel in the original remote sensing image in order to extract the spatial feature representation (Zhang et al., 2016a). As a result, 2-D CNN architectures are adopted, where the input data is a patch of  $P \times P$  neighboring pixels (Vetrivel et al., 2017; Chen et al., 2016; Hu et al., 2015a). In this sense, several methods have been implemented in order to extract high-level spatial features, as multi-scale image information (Liu et al., 2016; Zhao and Du, 2016a; Zhang et al., 2016b; Yu et al., 2017). For hyperspectral image

<sup>4</sup> Linear classifiers have an important limitation: these methods can only carve their input space into very simple regions (half-spaces) separated by a hyperplane (Chien, 1974).

<sup>5</sup> A DNN is a multi-layer perceptron (MLP) with many hidden and fully connected layers.

<sup>6</sup> RNNs can also be used as generative learning models if the output is not a label sequence associated with the input data sequence. Long short-term memory networks (LSTMs) are a kind of RNN (Hochreiter and Schmidhuber, 1997).

<sup>7</sup> CNNs can also work in unsupervised and semi-supervised mode (Dosovitskiy et al., 2014; Romero et al., 2016; Liu et al., 2017). On the other hand, recent efforts have resulted in deconvolutional neural networks (DCNN) (Zeiler et al., 2010). In Lu et al. (2017) authors combined the spatial pyramid model (SPM) with a shallow weighted DCNN to learn a set of feature maps and filters by minimizing the reconstruction error between the input image and the convolution result.

analysis normally it is necessary a pre-processing of the spectral information, with reduction of the number of bands for example (using, e.g., PCAs or autoencoders).

3. Extracting spectral-spatial information: the use of spatial features with spectral information in combined fashion can significantly improve the classification accuracy. When we talk about extracting spectral-spatial information with CNNs, two types of models can be highlighted:

- Those models that mix various techniques in addition to CNNs to extract spectral-spatial information separately and then combine them, for example using a 1-D CNN and 2-D CNN (Zhang et al., 2017; Yang et al., 2016) or combining different spectral feature extractors with spatial CNNs (Zhao and Du, 2016b). These methods do not take full advantage of the joint spatial/spectral correlation information.
- 3-D CNN architectures (Chen et al., 2016; Li et al., 2017) that compute each pixel in association with a  $P \times P$  spatial neighborhood and  $B$  spectral bands ( $P \times P \times B$ ). These models apply 3-D kernels in order to learn the local signal changes in both the spatial and the spectral domain of the hyperspectral data cubes, exploiting important discriminative information for classification and taking full advantage of the structural characteristics of the 3-D remote sensing data in general and hyperspectral images in particular (Li et al., 2017).

In this work, we propose an improved 3-D deep CNN model composed by 5 layers which uses all the spatial-spectral information of the hyperspectral image. We also include a specific strategy for management of the borders of the image and further develop an efficient implementation in graphics processing units (GPUs) to significantly speed up the computational performance. Deep Learning techniques, and in particular CNNs, involve a huge amount of matrix and vector operations. Most of these operations can be easily and massively parallelized using GPUs, due to their inherent design with hundreds/thousands of cores that can compute one or several matrix operations in parallel which, compared to a CPU with a few cores, results in a important decrease in computation time.

As a result, the main contributions of our work can be highlighted as follows: (1) the development of a new CNN architecture that considers the spatial and spectral information contained in hyperspectral images in simultaneous fashion, and (2) the development of an efficient implementation of the newly proposed architecture on GPUs that allows for efficient exploitation of the proposed methodology in real applications.

The remainder of the paper is organized as follows. Section 2 provides some general aspects about CNNs. Section 3 describes the proposed CNN. Section 4 validates the proposed approach by comparing it with classic ANNs such as the MLP and other CNN implementations in the literature, in order to illustrate the advantages of the proposed implementation in terms of both computational efficiency and classification accuracy. Section 5 concludes the paper with some remarks and hints at plausible future research lines.

## 2. CNNs

CNNs are composed by a set of blocks that can be applied both across space and across time (images, audio and video signals). Each block transforms the input volume to an output volume of neuron activations which will serve as input to the next block. In contrast to conventional ANNs, the blocks of neurons in CNNs operate like kernels which are connected and applied over one patch of the input volume (see Fig. 1), that is, the neurons of a block

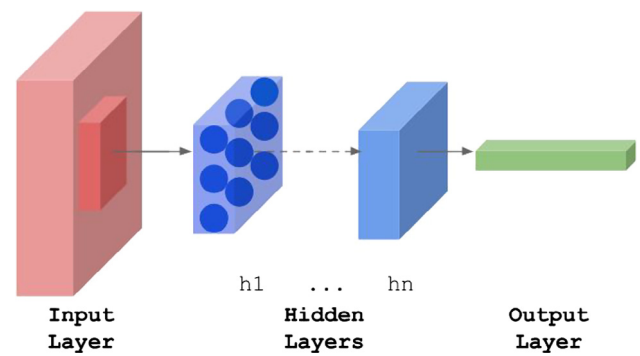


**Fig. 1.** CNN architecture. Each block or layer of a CNN transforms the input volume to an output volume of neuron activations. Neurons in layer  $l$  are connected to a small region of layer  $l - 1$ .

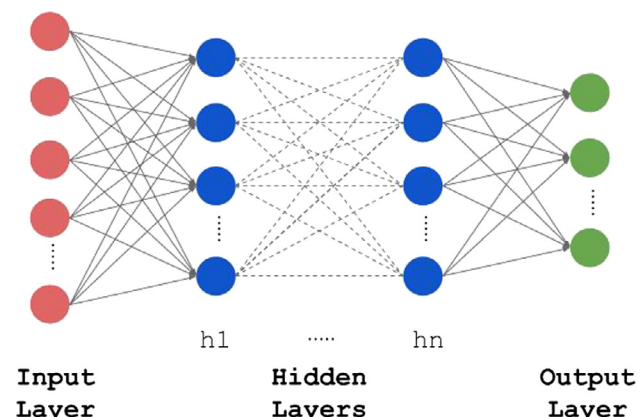


**Fig. 2.** MLP architecture. All nodes in one layer are fully connected with the nodes of the previous layer.

are not fully-connected to all neurons of the previous layer as in the standard MLP (see Fig. 2). These blocks actually compose feature extraction stages, which specifically consist of three layers (Zhang et al., 2016a) that are the key parts of almost all CNN models:

1. Convolution layer: a 3-D layer where each neuron computes the dot product between its weights and a small region of the input volume, i.e. a rectangular section of the previous layer, to which it is connected. Its goal is to identify certain features from the previous layer and mapping their appearance to a feature map (LeCun et al., 2015). We can see this layer as set of  $k$  filters of size  $l \times l \times q$  (filter bank) where the neurons share the same weights and bias and connect the input volume to the output volume (Zhang et al., 2016a). Each filter detects a particular feature at every location on the input. The resulting output volume of the layer  $l$  is a feature map of size  $d^l \times d^l \times k^l$  that stores the information where the feature occurs in the original input volume and is calculated as  $z_i^l = B^l + \sum_{j=1}^{k^{l-1}} W_{ij}^l * z_j^{l-1}$ , where  $i \in [1, k^l]$ ,  $B^l$  is the bias matrix of layer  $l$  and  $W_{ij}^l$  is the weight matrix or filter (also known as kernel or feature detector)<sup>8</sup> that connects the  $j$ th feature map in layer  $l - 1$  ( $z_j^{l-1}$ ) with the  $i$ th feature map in layer  $l$ .

<sup>8</sup> The concept of weight matrix can be understood as a feature detector or filter which can be used to search for a specific spatial characteristic of the input data. The weight matrix will assign a greater weight to the pixels that collect this characteristic penalizing the pixels that do not exhibit this spatial behaviour.

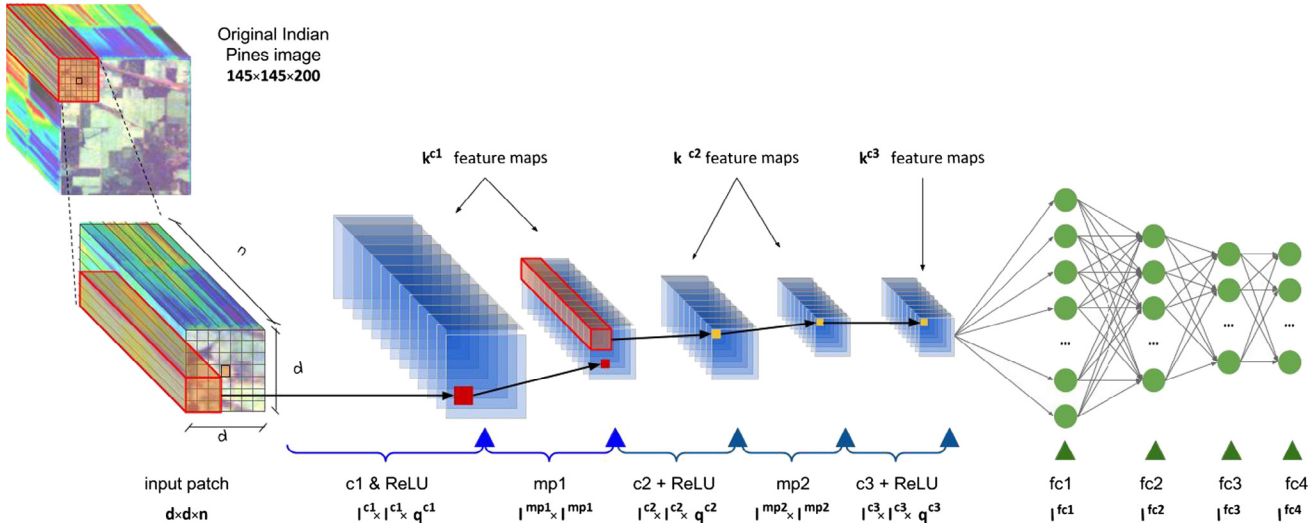


Fig. 3. Proposed CNN architecture.

2. Nonlinearity layer: this layer embeds a nonlinear function (as the rectified linear unit or ReLU). [Jarrett et al. \(2009\)](#), [Nair and Hinton \(2010\)](#), and [Glorot et al. \(2011\)](#) that is applied to each feature map's component in order to learn nonlinear representations:  $a^l = f(z^l)$ .
3. Pooling layer: this layer is used to make the features invariant from the location and to summarize the output of multiple neurons in convolution layers through a pooling function. In our case, this layer executes a max operation within a small spatial region  $R$  over the resulting feature map after the nonlinearity layer:  $p^l = \max_{i \in R} a_i^l$ .

Sparse connectivity and shared weights make CNNs ideal for processing and classifying images, reducing the number of parameters to be learned by the network and ensuring some degree of shift, scale, and distortion in-variance.

### 3. Proposed CNN

The structure of our new CNN is shown in Fig. 3. As we can see, our CNN consists of an input layer, three convolution layers with ReLU as nonlinear activation function, two maxpool layers, and four fully-connected layers. The last one is the output layer which obtains the desired label for the input data. In the following, we first provide details about our preprocessing strategy for hyperspectral data, particularly to account for spatial information, prior to feeding this information to the CNN. Then, we provide a detailed explanation about the considered architecture.

#### 3.1. Data preprocessing

Normally, CNNs receive a complete normalized image prior to classification. However, in hyperspectral images the classes are

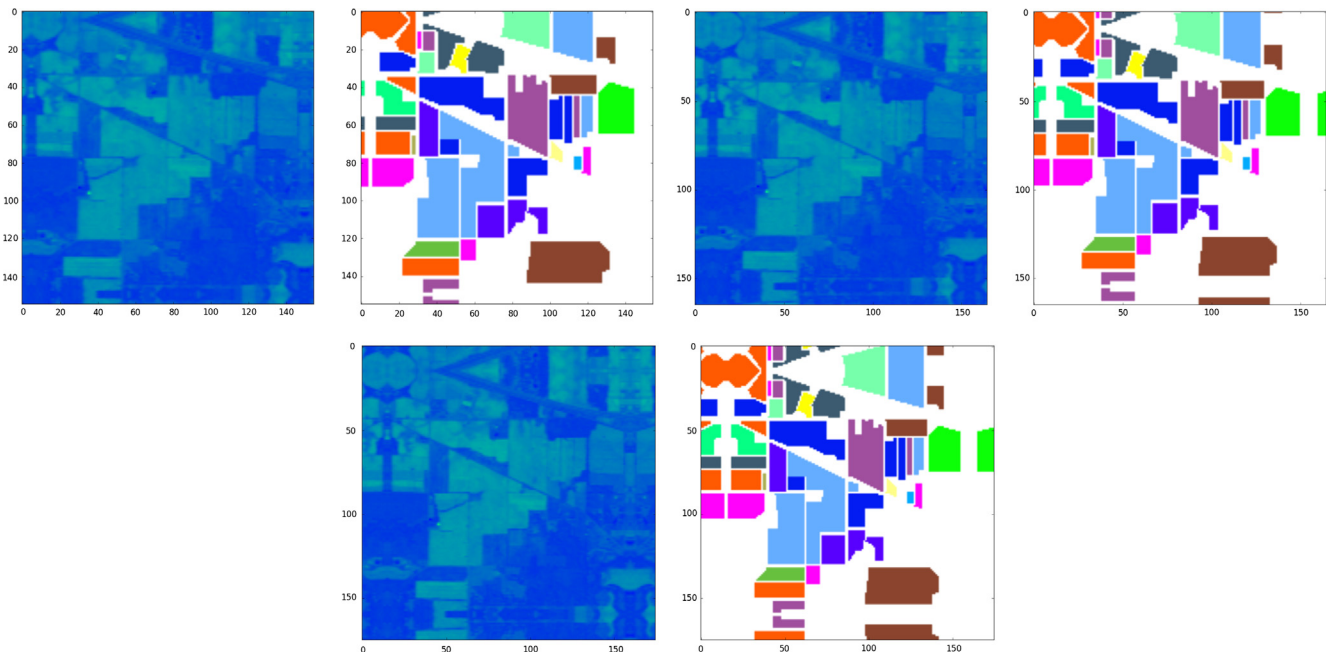


Fig. 4. Graphical illustration of our border mirroring strategy (with  $d = 9, d = 19$  and  $d = 29$ ) using the well-known AVIRIS Indian Pines hyperspectral image (and its associated ground-truth) as an example.

typically mixed within the image, so we feed the pixel (vectors) one by one to the network. This allows exploiting the rich spectral information contained in the hyperspectral data, but we need an additional mechanism in order to include also the spatial information.

To achieve this and take advantage of both the spatial and the spectral information simultaneously, we have implemented a 3-D approach in which we feed the network with a neighborhood window centered around each pixel vector. In this way, the input layer accepts volumes of size  $d \times d \times n$ , where  $d$  is the width and height of the input volume and  $n$  is the total number of bands of the original hyperspectral image. This requires a pre-processing stage to divide the hyperspectral image into patches of size  $d \times d \times n$ . The desired label to be reached by the network will be the one that owns the central pixel of the patch  $[d/2 + 1, d/2 + 1, n]$ .

However, this preprocessing strategy faces a problem: for the pixels belonging to the borders of the image a  $d \times d$  surrounding neighborhood cannot be defined. As we increase  $d$ , we cannot properly account for the border information around some pixels. Some approaches simply disregard those border pixels for which they do not have spatial neighbours. This supposes a significant loss of samples that, together with the scarcity of the samples, can make the network result in overfitting. In order to avoid this problem, we have implemented a simple algorithm to replicate borders that allows us to feed the net with all the border pixels and to use them as any other pixel in the image. In this way, we can classify the complete hyperspectral image by replicating the pixels near the border, i.e. mirroring the  $d/2$  pixels of border outwards, in order to create the corresponding patches or windows of the original border pixels, as illustrated graphically in Fig. 4 using the well-known AVIRIS Indian Pines hyperspectral image (described in detail in Section 4).

### 3.2. CNN architecture details

Once the edges are replicated and the hyperspectral image is split into 3-D patches, these are grouped in batches of size  $b$  and sent to the CNN. Then, the  $d \times d \times n$  patches are sent as input volume to the first convolution layer ( $c1$ ), composed by  $k^c1$  filters of  $l^c1 \times l^c1 \times q^c1$ , where  $q^c1 = n$ , the stride is fixed to 1, and there is no padding.

After applying the ReLU function, the  $k^c1$  feature maps generated by  $c1$  are sent to the first MaxPool layer ( $mp1$ ), with a  $l^{mp1} \times l^{mp1}$  kernel, stride of 2, and padding. The resulting output volume  $p^{mp1} = d^{mp1} \times d^{mp1} \times k^c1$  is sent to the second convolution layer ( $c2$ ) with  $k^c2$  filters of size  $l^c2 \times l^c2 \times q^c2$ , where  $q^c2 = k^c1$ , with the same stride as in the first convolution and no padding either.

Again, after applying the ReLU function, the  $k^c2$  feature maps generated by  $c2$  are sent to the second MaxPool layer ( $mp2$ ), with a  $l^{mp2} \times l^{mp2}$  kernel, stride of 2 and padding. The resulting output volume  $p^{mp2} = d^{mp2} \times d^{mp2} \times k^c2$  is sent to the last convolution layer ( $c3$ ), that has  $k^c3$  filters of size  $l^c3 \times l^c3 \times q^c3$ . This layer has the purpose of further refining the feature maps by processing each element one by one, so  $k^c3 = q^c3 = k^c2$  and  $l^c3 = 1$ . There is no third maxpool layer, so the output volume is reshaped in order to send it to fully-connected layers.

Four fully-connected layers were implemented ( $fc1, fc2, fc3$  and  $fc4$ ) with  $l^{fc1}, l^{fc2}, l^{fc3}$  and  $l^{fc4}$  nodes, respectively. The first three fully-connected layers compute their output as  $y^{fc} = f(w^{fc}y^{fc-1} + b^{fc})$ , where  $w^{fc}$  are their weight matrices,  $b^{fc}$  are their bias vectors,  $y^{fc-1}$  is the output of the previous layer (in the first case,  $y^{fc-1} = p^{c3}$ , i.e. the output of  $C3$  layer) and the activation

function  $f(\cdot)$  is ReLU. Finally, the last resulting matrix  $y^{fc3}$  is sent to  $fc4$ , which computes the outputs of the network with a softmax function as  $y^{fc4} = w^{fc4}y^{fc3} + b^{fc4}$ , where  $y^{fc4}$  contains the desired labels for the original  $d \times d \times n$  input data.

In Algorithm 1 we can see a scheme of the operation of the proposed method. As we can notice, the method uses cross-entropy in order to determine the loss of the CNN model. It is defined as  $H_y(y) = \sum_i y'_i \log(y_i)$ , where  $y$  is our predicted probability distribution and  $y'$  is the true distribution, so the cross-entropy is a measure of how inefficiently predictions are calculated for describing the truth.

### Algorithm 1. Proposed CNN method

---

```

1: procedure CNN_method( $Y \rightarrow$  original hyperspectral
   image)
2:    $max\_epochs \rightarrow$  Set number of epochs value
3:    $max\_iters \rightarrow$  Set number of iterations value
4:    $d \rightarrow$  Set patch size value
5:    $n = Y.bands$ 
6:    $Y_{norm} = band\_mean\_normalize(Y)$ 
7:    $Y' = border\_mirroring(Y_{norm}, d) \rightarrow$  mirroring of  $d$  border
   pixels
8:    $P = patches\_creation(Y', d, n) \rightarrow$  splitting  $Y'$  into patches
   of  $d \times d \times n$ 
9:    $T_a, T_b = training\_test\_sets(P) \rightarrow$  training  $T_a$  and testing
    $T_b$  sets
10:   $G = batches\_creation(T_a, b) \rightarrow$  grouping patches in
    batches of size  $b$ 
11:  for  $e < max\_epochs$  do
12:    for  $it < max\_iters$  do
13:       $G' = get\_next\_batch(G)$ 
14:       $labels\_G'.predicted = forward\_pass(G')$ 
15:       $error = cross\_entropy(labels\_G', labels\_G'.predicted)$ 
16:       $W, B = optimizer(error)$ 
17:    end for
18:  end for
19: end procedure

```

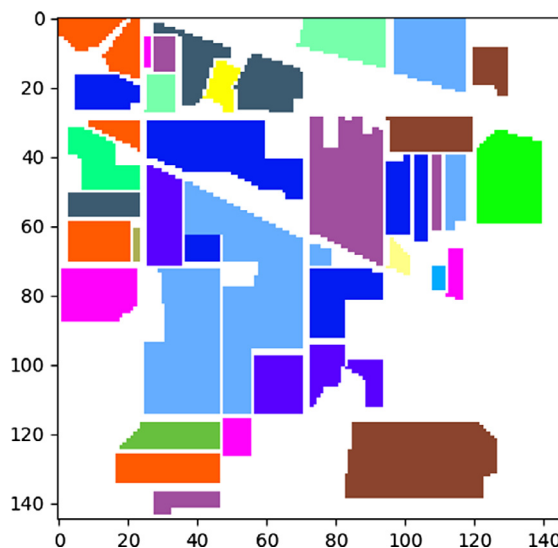
---

As an interesting point we note that, for the initialization of all weights and bias of the network, we have used the so-called Xavier initializer (Glorot and Bengio, 2010), that allows the network to achieve greater stability, and the Adagrad optimizer (Duchi et al., 2011), as a simple method for learning rate adaptation. All the network characteristics (weights and bias initialization, optimizer, learning rate, steps, kernels size, use of padding and size of strides) are configurable through a JavaScript Object Notation (JSON)<sup>9</sup> file, as well as parameters  $d$  and  $b$ , which makes the implementation of the network flexible and easy to modify. Such implementation has been performed in Python.<sup>10</sup> In this way, the CNN takes advantage of the information of the central pixel neighbors as well as all the available spectral information, being able to adapt its structure easily and quickly.

As we anticipated in Section 3.1, this kind of networks may suffer from an overfitting problem because of the complexity of the model derived from the large number of parameters that must be learned, and a lack of training samples (that is quite common in remote sensing applications). This problem may result in poor predictive performance in the testing phase, despite a high accuracy can be obtained in the training phase. To avoid such

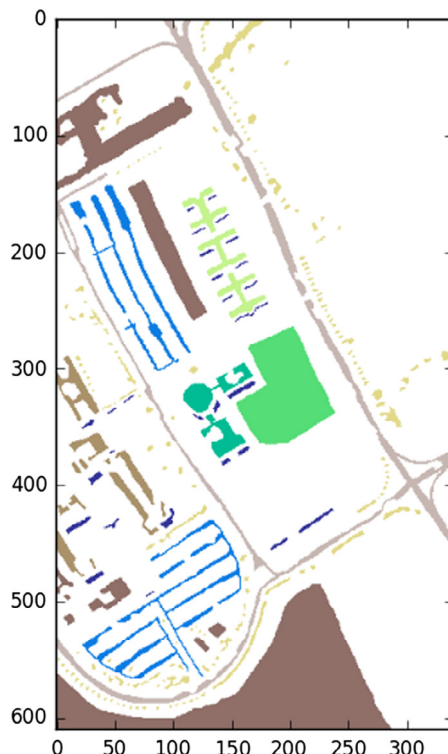
<sup>9</sup> <http://www.json.org/>.

<sup>10</sup> <https://www.python.org/>.



Color	Land cover type	Samples
Background	Background	10776
Yellow	Alfalfa	46
Blue	Corn-notill	1428
Orange	Corn-min	830
Green	Corn	237
Magenta	Grass/Pasture	483
Purple	Grass/Trees	730
Cyan	Grass/Pasture-mowed	28
Light Green	Hay-windrowed	478
Brown	Oats	20
Dark Blue	Soybeans-notill	972
Dark Green	Soybeans-min	2455
Dark Cyan	Soybeans-clean	693
Dark Purple	Wheat	205
Dark Brown	Woods	1265
Light Blue	Bldg-Grass-Tree-Drives	386
Yellow	Stone-steel towers	93
Total samples		21025

Fig. 5. Original ground-truth image of the AVIRIS Indian Pines scene and number of samples per class.



Color	Land cover type	Samples
Grey	Background	164624
Dark Grey	Asphalt	6631
Dark Brown	Meadows	18649
Brown	Gravel	2099
Yellow	Trees	3064
Light Green	Painted metal sheets	1345
Green	Bare Soil	5029
Cyan	Bitumen	1330
Blue	Self-Blocking Bricks	3682
Dark Blue	Shadows	947
Total samples		207400

Fig. 6. Original ground-truth image of the ROSIS University of Pavia scene and number of samples per class.

overfitting problems, we have allowed an optional and configurable dropout mechanism in the first and second convolution layers. The dropout method sets the output of some randomly selected hidden neurons to zero, so that the dropped neurons do not contribute in the forward pass and they are not used in the back-propagation stage (Hinton et al., 2012).

To conclude this section, it is important to note that the proposed CNN has been implemented using the TensorFlow open source library for machine intelligence<sup>11</sup> including its GPU func-

tionalities, that allow for fast performance even when dealing with very large hyperspectral image volumes. In the following section, we evaluate the proposed CNN from the viewpoint of both computational performance and classification accuracy.

## 4. Experiments and results

### 4.1. Experimental configuration

In order to evaluate the performance of our newly presented CNN architecture, we use a hardware environment composed by

<sup>11</sup> <https://www.tensorflow.org>.

a 6th Generation Intel® Core™ i7-6700 K processor with 8 M of Cache and up to 4.20 GHz (4 cores/8 way multitask processing), 40 GB of DDR4 RAM with a serial speed of 2400 MHz, a GPU NVIDIA GeForce GTX 1080 with 8 GB GDDR5X of video memory and 10Gbps of memory frequency, a Toshiba DT01ACA HDD with 7200RPM and 2 TB of capacity, and an ASUS Z170 pro-gaming motherboard.

#### 4.2. Hyperspectral image data

In our experiments, we have used two well-known hyperspectral image data sets. The first one is the Indian Pines image, gathered in 1992 by the Airborne Visible/Infrared Imaging Spectrometer (AVIRIS) sensor (Green et al., 1998) over a set of agricultural fields with regular geometry and with a multiple crops and

**Table 1**

Indian Pines: number of samples in the training set used by the proposed method and by the method in Chen et al. (2016).

Indian Pines					
clase	pixels	200 samples per class	100 samples per class	50 samples per class	Chen et al. (2016)
Alfalfa	46	33	33	33	30
Corn-notill	1428	200	100	50	150
Corn-min	830	200	100	50	150
Corn	237	181	100	50	100
Grass/pasture	483	200	100	50	150
Grass/trees	730	200	100	50	150
Grass/pasture-mowed	28	20	20	20	20
Hay-windrowed	478	200	100	50	150
Oats	20	14	14	14	15
Soybeans-notill	972	200	100	50	150
Soybeans-min	2455	200	100	50	150
Soybeans-clean	593	200	100	50	150
Wheat	205	143	100	50	150
Woods	1265	200	100	50	150
Bldg-grass-tree-drives	386	200	100	50	50
Stone-steel towers	93	75	75	50	50
Total	10249	2466	1342	717	1765

**Table 2**

University of Pavia: number of samples in the training set used by the proposed method and by the method in Chen et al. (2016).

Pavia University					
class	pixels	200 samples per class	100 samples per class	50 samples per class	Chen et al. (2016)
Asphalt	6631	200	100	50	548
Meadows	18649	200	100	50	540
Gravel	2099	200	100	50	392
Trees	3064	200	100	50	542
Painted metal sheets	1345	200	100	50	256
Bare soil	5029	200	100	50	532
Bitumen	1330	200	100	50	375
Self-blocking bricks	3682	200	100	50	514
Shadows	947	200	100	50	231
Total	42776	1800	900	450	3930

**Table 3**

Configuration of the CNN architecture for the Indian Pines and University of Pavia datasets. The kernel size (like the number and type of layers, strides and padding) is one of the design choices of the proposed CNN architecture. Large kernels allow our CNN to learn more complex features, although with larger kernels the computational time of the training/testing phase is also greater.

Hyperspectral datasets	CNN proposed topologies					Fully Connected Layers		
	Kernel size $k^c \times l^c \times l^c \times q^c$	ReLU	Pooling $l^{mp} \times l^{mp}$	Dropout	Nºneurons $l^c$			
Indian Pines	600 × 5 × 5 × 200	Yes	2 × 2	Yes (10%)	1024	ReLU	Yes(10%)	
	200 × 3 × 3 × 600	Yes	2 × 2	Yes (10%)	1024	ReLU	No	
	200 × 1 × 1 × 200	Yes	No	No	512	ReLU	No	
Pavia University	380 × 7 × 7 × 103	Yes	2 × 2	Yes(20%)	2048	ReLU	No	
	350 × 5 × 5 × 380	Yes	2 × 2	Yes(20%)	2048	ReLU	No	
	350 × 1 × 1 × 350	Yes	No	No	1024	ReLU	No	
					9	Softmax	No	
Common parameters								
Bach size b	Steps (iterations)	Epochs	Learning rate	Optimizer				
100	1500	20	0.01	AdagradOptimizer				

irregular patches of forest in Northwestern Indiana. The AVIRIS Indian Pines scene has  $145 \times 145$  pixels with 224 spectral bands in the range from 400 to 2500 nm, with 10 nm of spectral resolu-

tion, 20 m moderate spatial resolution, and 16 bits radiometric resolution. After an initial analysis, 4 zero bands and another 20 bands with lower signal-to-noise ratio (SNR) have been removed because

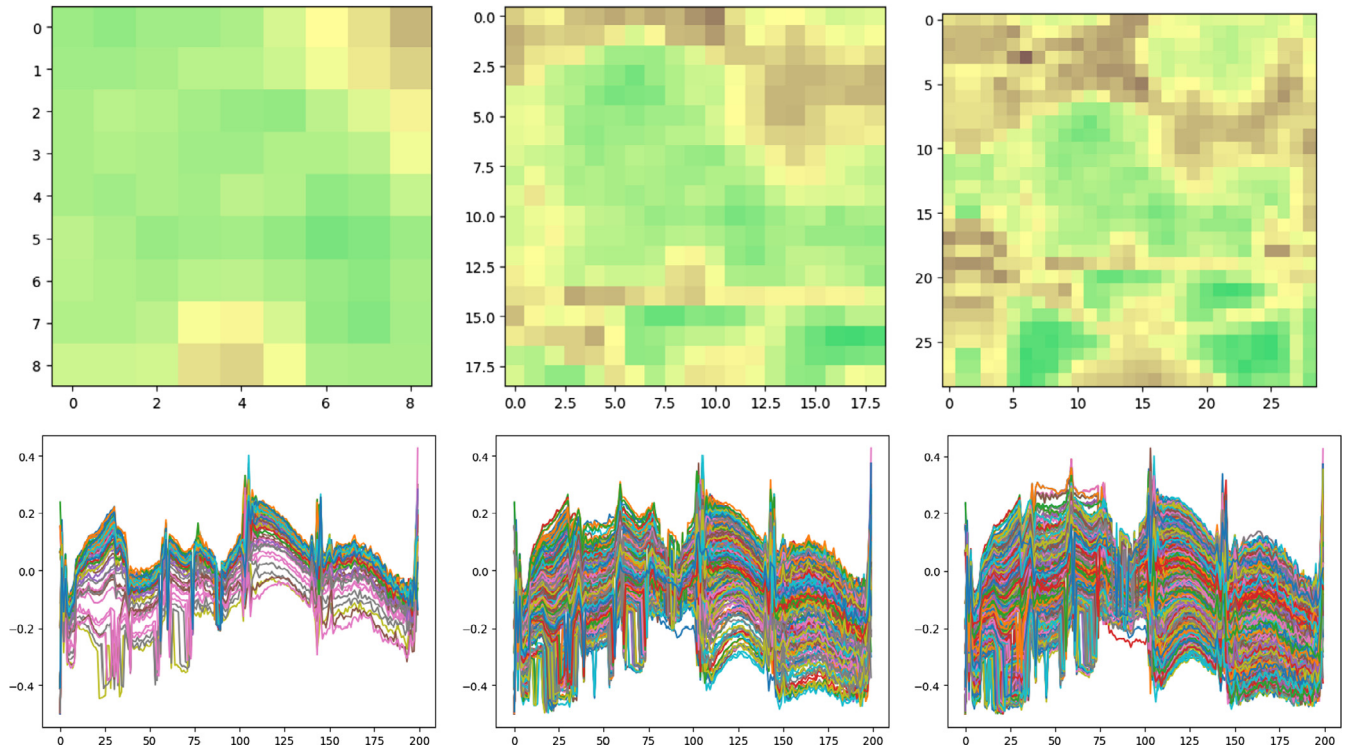


**Fig. 7.** Illustration of the effect of using different patch sizes for the Indian Pines scene. The upper row shows the size of the neighborhood around the central pixel when we use  $d = 9$ ,  $d = 19$  and  $d = 29$ , as we can see on the axes from left to right (color map of band 140). In the lower row we can see the spectral signature of the pixels that form each neighborhood, respectively. (For interpretation of the references to color in this figure legend, the reader is referred to the web version of this article.)

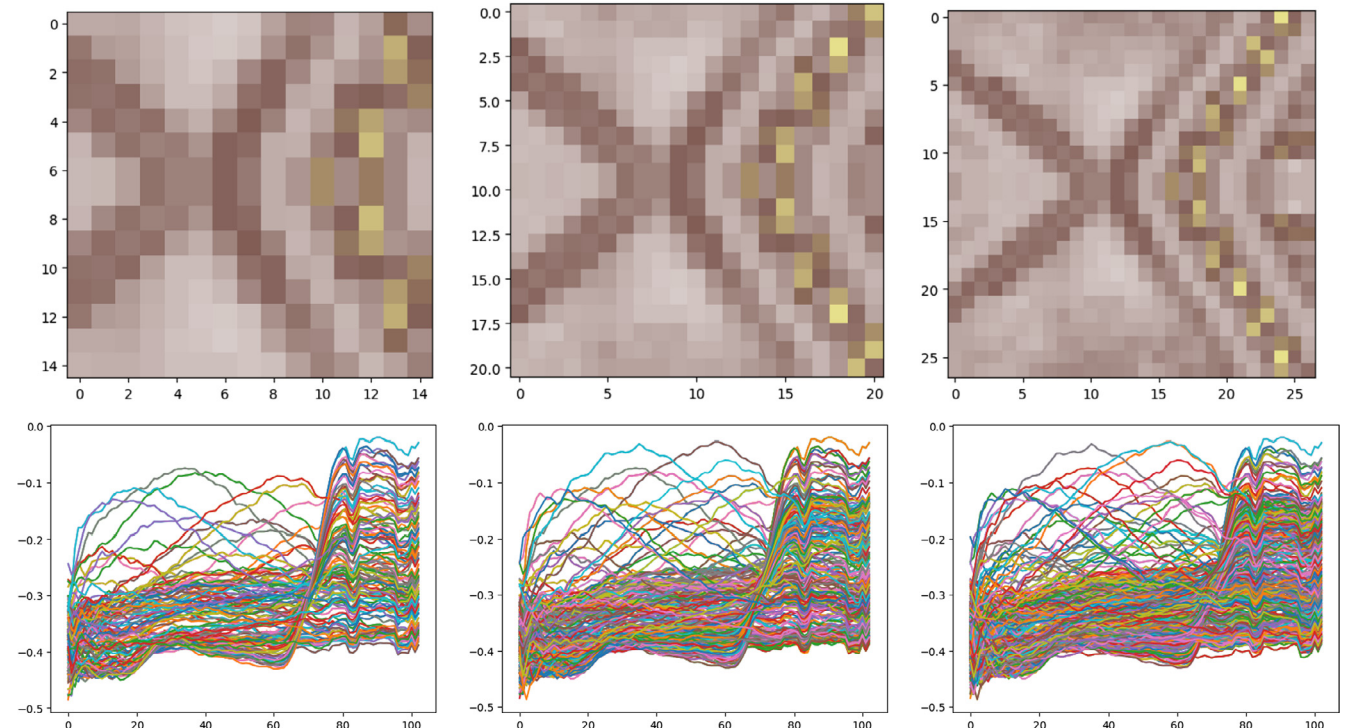


**Fig. 8.** Illustration of the effect of using different patch sizes for the University of Pavia scene. The upper row shows the size of the neighborhood around the central pixel when we use  $d = 15$ ,  $d = 21$  and  $d = 27$ , as we can see on the axes from left to right (color map of band 10). In the lower row we can see the spectral signature of the pixels that form each neighborhood, respectively. (For interpretation of the references to color in this figure legend, the reader is referred to the web version of this article.)

of atmospheric absorption phenomena in those bands, retaining only 200 spectral channels. Moreover, about half of the pixels in the hyperspectral image (10249 of 21025, i.e. 48.74%) contain ground-truth information, which comes in the form of a single

label assignment for each pixel with a total of 16 ground-truth classes (see Fig. 5).

The second data set used in experiments was collected by the Reflective Optics System Imaging Spectrometer (ROSIS) sensor

**Table 4**

Execution times (in seconds) and accuracies measured with patches of size  $d = 9$ ,  $d = 19$  and  $d = 29$  for the Indian Pines dataset and  $d = 15$ ,  $d = 21$  and  $d = 27$  for the University of Pavia dataset. The CNN configuration is the one indicated in Table 3, with 1500 iterations, 100 samples per class and 5 executions.

Dataset	Patch size	Time per step		Total time		Accuracy	
		Avg.	Std. dev.	Avg.	Std. dev.	Avg.	Std. dev.
Indian Pines	$d = 9$	0.02	0.01	29.22	1.05	78.46	4.45
	$d = 19$	0.08	0.02	116.30	3.22	91.34	1.59
	$d = 29$	0.16	0.03	248.29	7.91	95.53	0.48
University of Pavia	$d = 15$	0.02	0.01	34.78	1.13	94.02	0.62
	$d = 21$	0.05	0.02	74.66	2.22	95.08	1.41
	$d = 27$	0.09	0.02	131.66	2.88	94.13	0.66

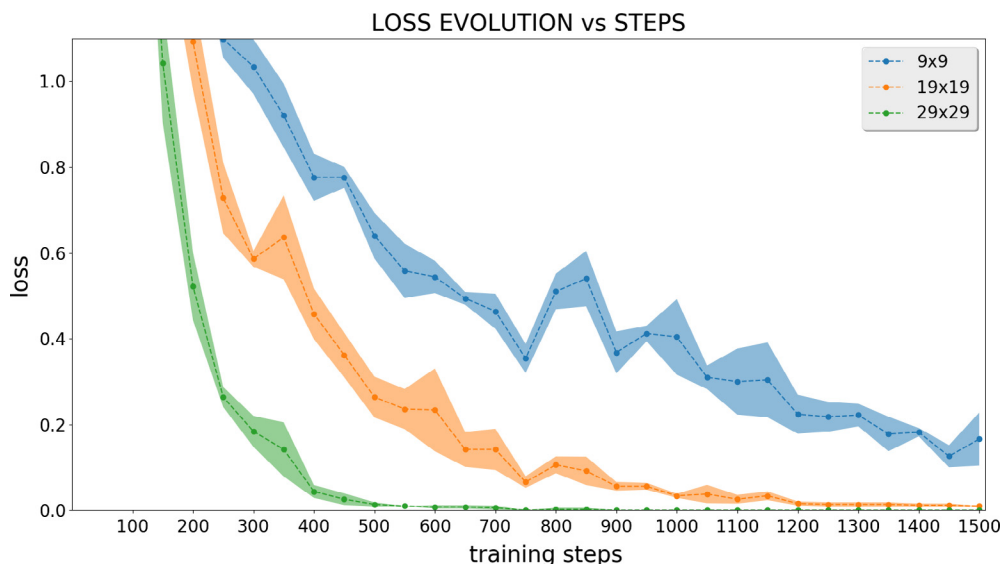


**Fig. 9.** Indian Pines: Evolution of the validation loss in terms of steps (iterations) with  $d = 9$ ,  $d = 19$  and  $d = 29$ . The shadow shows the standard deviation of the loss for the five executions of each patch (zoom in error interval [0, 1]). This experiment has been executed using 1500 iterations.

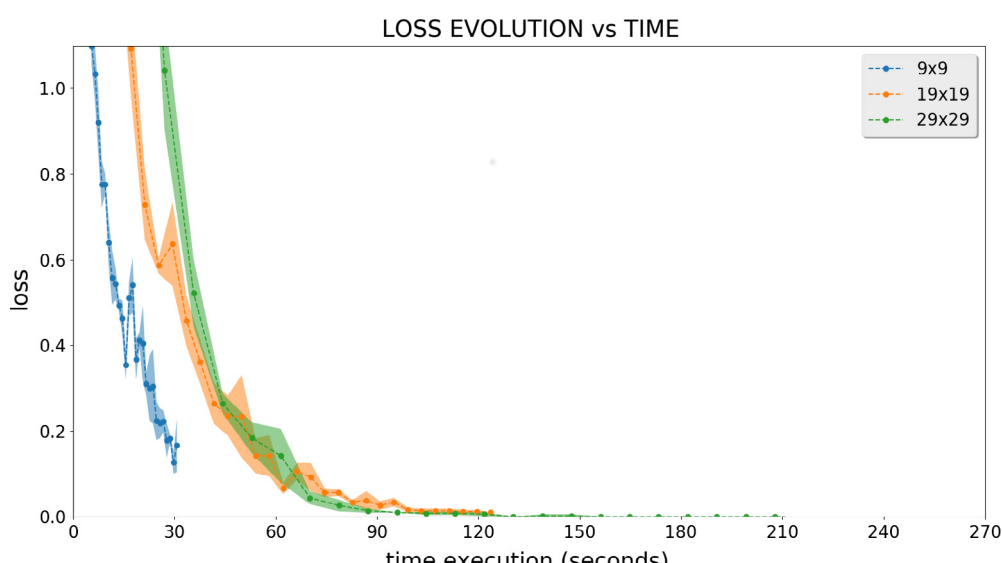


**Fig. 10.** Indian Pines: Evolution of the validation loss in terms of time (seconds) with  $d = 9$ ,  $d = 19$  and  $d = 29$ . The shadow shows the standard deviation of the loss for the five executions of each patch (zoom in error interval [0, 1]). This experiment has been executed using 1500 iterations.

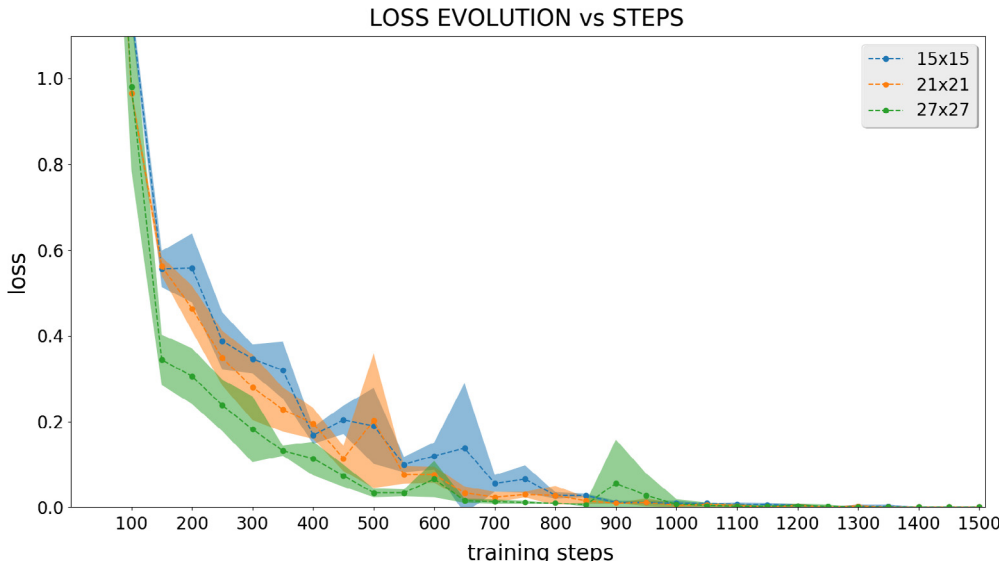


**Fig. 11.** Pavia University: Evolution of the validation loss in terms of steps (iterations) with  $d = 15$ ,  $d = 21$  and  $d = 27$ . The shadow shows the standard deviation of the loss for the five executions of each patch (zoom in error interval  $[0, 1]$ ). This experiment has been executed using 1500 iterations.

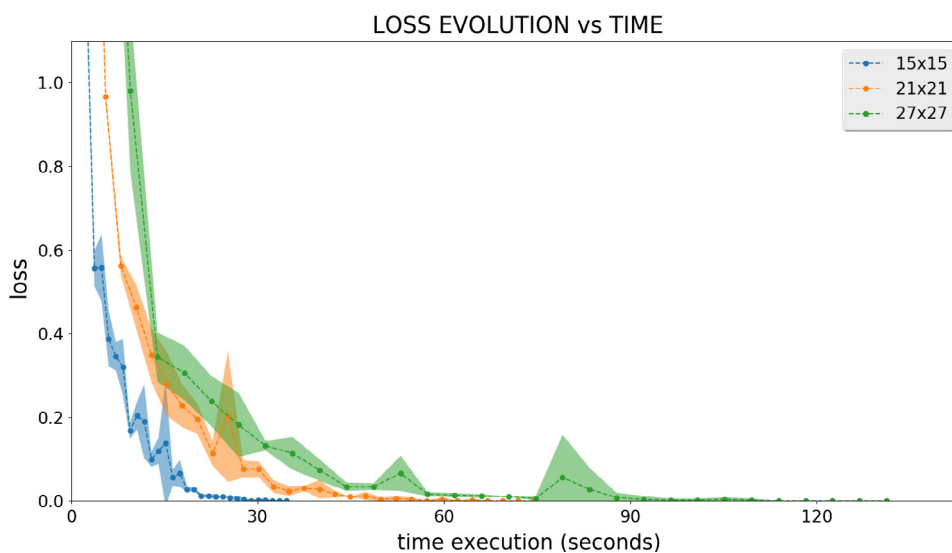


**Fig. 12.** Pavia University: Evolution of the validation loss in terms of time (seconds) with  $d = 15$ ,  $d = 21$  and  $d = 27$ . The shadow shows the standard deviation of the loss for the five executions of each patch (zoom in error interval  $[0, 1]$ ). This experiment has been executed using 1500 iterations.

(Kunkel et al., 1988) during a flight campaign over the city of Pavia, in northern Italy. The dataset covers an urban environment, with various solid structures (asphalt, gravel, metal sheets, bitumen, bricks), natural objects (trees, meadows, soil), and shadows (9 classes in total). Other objects whose compositions differ from the labeled ones are considered as clutter. The scene was collected over an university area. It contains 103 spectral bands with  $610 \times 340$  pixels in the spectral range from 0.43 to 0.86  $\mu\text{m}$ , and spatial resolution of 1.3 m/pixel. About 20.62% of the pixels in the hyperspectral image (42776 of 207400) contain ground-truth information (see Fig. 6).

#### 4.2.1. Data preprocessing: division of training and testing sets

When our method divides the hyperspectral images into training and testing sets, it follows a method of preprocessing with class balancing that must be conveniently explained at this point. In addition to their huge dimensionality and the existing correlation between the spectral features collected (Melgani and Bruzzone,

2004), hyperspectral images present another complication: the class imbalance problem (He and Garcia, 2009). This problem appears in a dataset when some of the classes are heavily under-represented (in terms of their labeled samples) as compared to other classes (García et al., 2011), leading to poor classification performance in many real-world applications, especially for the minority classes. In order to deal with this problem, and taking into account that we could not identify a common pattern about sample selection strategies in the literature, we have tried to keep a stratified sampling strategy in our experiments. As a result, we tried to balance the number of samples selected in accordance with the number of available samples per class.

The first step is to divide randomly the original dataset in two subsets: the first one (training set) with 75%<sup>12</sup> of the samples and the second one (testing set) with the remaining 25%. If we keep that

<sup>12</sup> For each class we make sure that about 75% of each class is taken, until we have a number of samples close to 75% of the complete dataset, so we make sure that all classes are represented in the subset.

75% of samples for the training set, we will once again experience the class imbalance problem. For instance, in the Indian Pines image the Alfalfa class has only 46 samples as opposed to Corn-notill,

which has 1428. 75% of each is 34,5 ≈ 36 for Alfalfa and 1071 for Corn-notill, a completely unbalanced result. The solution adopted in this case is to simply reduce the number samples until a balanced

**Table 5**

Classification accuracies obtained by our CNN (with patch sizes of  $d = 9$ ,  $d = 19$  and  $d = 29$ ) for the Indian Pines hyperspectral dataset. We used 2500 iterations and repeated the experiment 5 times.

Neural networks	CNN $d = 9$			CNN $d = 19$			CNN $d = 29$		
	Samples per class	50	100	200	50	100	200	50	100
Alfalfa	98.70 (1.06)	99.13 (1.06)	99.13 (1.06)	99.57 (0.87)	100.00 (0.00)	99.57 (0.87)	99.13 (1.74)	99.57 (0.87)	99.13 (1.06)
Corn-notill	70.76 (3.42)	76.93 (2.50)	80.48 (9.37)	76.74 (3.89)	85.84 (1.92)	94.47 (2.46)	82.10 (3.94)	91.32 (0.46)	98.17 (0.67)
Corn-min	78.92 (5.37)	90.55 (1.97)	96.65 (1.20)	82.77 (2.61)	93.23 (2.09)	98.22 (0.87)	86.41 (4.29)	94.84 (0.47)	98.92 (0.68)
Corn	96.54 (1.89)	99.75 (0.21)	99.66 (0.17)	99.41 (0.83)	99.66 (0.32)	100.00 (0.00)	97.81 (2.92)	100.00 (0.00)	100.00 (0.00)
Grass/Pasture	89.86 (4.56)	97.81 (0.81)	99.46 (0.52)	95.20 (1.54)	98.18 (0.73)	99.75 (0.20)	96.15 (3.75)	98.34 (1.23)	99.71 (0.21)
Grass/Trees	97.40 (0.94)	98.11 (0.88)	99.53 (0.32)	92.96 (2.64)	97.92 (1.31)	98.90 (0.43)	96.47 (2.43)	98.66 (0.94)	99.40 (0.52)
Grass/pasture-mowed	100.00 (0.00)	100.00 (0.00)	100.00 (0.00)	100.00 (0.00)	100.00 (0.00)	100.00 (0.00)	100.00 (0.00)	100.00 (0.00)	100.00 (0.00)
Hay-windrowed	99.29 (0.34)	99.62 (0.08)	99.67 (0.21)	99.12 (1.06)	99.08 (0.45)	99.62 (0.47)	99.62 (0.50)	99.96 (0.08)	100.00 (0.00)
Oats	100.00 (0.00)	100.00 (0.00)	100.00 (0.00)	100.00 (0.00)	100.00 (0.00)	100.00 (0.00)	100.00 (0.00)	100.00 (0.00)	100.00 (0.00)
Soybeans-notill	80.39 (3.52)	87.86 (1.95)	92.43 (2.03)	88.35 (4.26)	94.81 (1.94)	98.00 (0.78)	88.66 (1.62)	95.21 (1.26)	98.62 (1.39)
Soybeans-min	65.82 (5.83)	79.45 (1.74)	76.42 (4.61)	69.52 (3.63)	85.85 (1.35)	94.32 (2.02)	79.40 (1.33)	90.52 (1.16)	96.15 (0.57)
Soybean-clean	80.84 (4.29)	90.96 (3.58)	97.74 (0.86)	84.65 (3.19)	96.90 (1.61)	99.09 (0.45)	88.67 (1.80)	97.17 (1.64)	99.33 (0.18)
Wheat	99.61 (0.78)	99.80 (0.39)	99.71 (0.24)	99.90 (0.20)	99.90 (0.20)	100.00 (0.00)	99.32 (0.39)	100.00 (0.00)	99.90 (0.20)
Woods	91.21 (1.17)	94.80 (1.43)	97.71 (0.74)	88.35 (3.57)	95.54 (1.43)	98.85 (0.94)	96.74 (1.22)	98.12 (0.54)	98.96 (0.46)
Bldg-Grass-Tree-Drives	91.14 (2.07)	98.50 (0.81)	99.27 (0.60)	96.94 (3.11)	98.81 (1.42)	99.90 (0.13)	99.07 (0.26)	99.69 (0.25)	100.00 (0.00)
Stone-steel towers	100.00 (0.00)	100.00 (0.00)	100.00 (0.00)	99.57 (0.86)	100.00 (0.00)	100.00 (0.00)	99.78 (0.43)	98.92 (0.96)	100.00 (0.00)
Overall Accuracy	80.85 (1.58)	88.46 (0.32)	90.11 (0.67)	83.73 (1.30)	92.54 (0.16)	97.23 (0.30)	88.78 (0.78)	95.05 (0.28)	98.37 (0.17)
Average Accuracy	90.03 (0.98)	94.58 (0.22)	96.12 (0.28)	92.07 (0.66)	96.61 (0.24)	98.79 (0.10)	94.33 (0.35)	97.64 (0.13)	99.27 (0.11)
Kappa	78.44 (1.74)	86.92 (0.36)	88.81 (0.76)	81.68 (1.44)	91.54 (0.18)	96.85 (0.34)	87.31 (0.88)	94.38 (0.31)	98.15 (0.19)
Run time	47.97 (0.01)	48.50 (0.01)	48.21 (0.01)	193.40 (0.01)	192.85 (0.01)	197.65 (0.01)	421.07 (0.02)	404.15 (0.02)	405.46 (0.02)

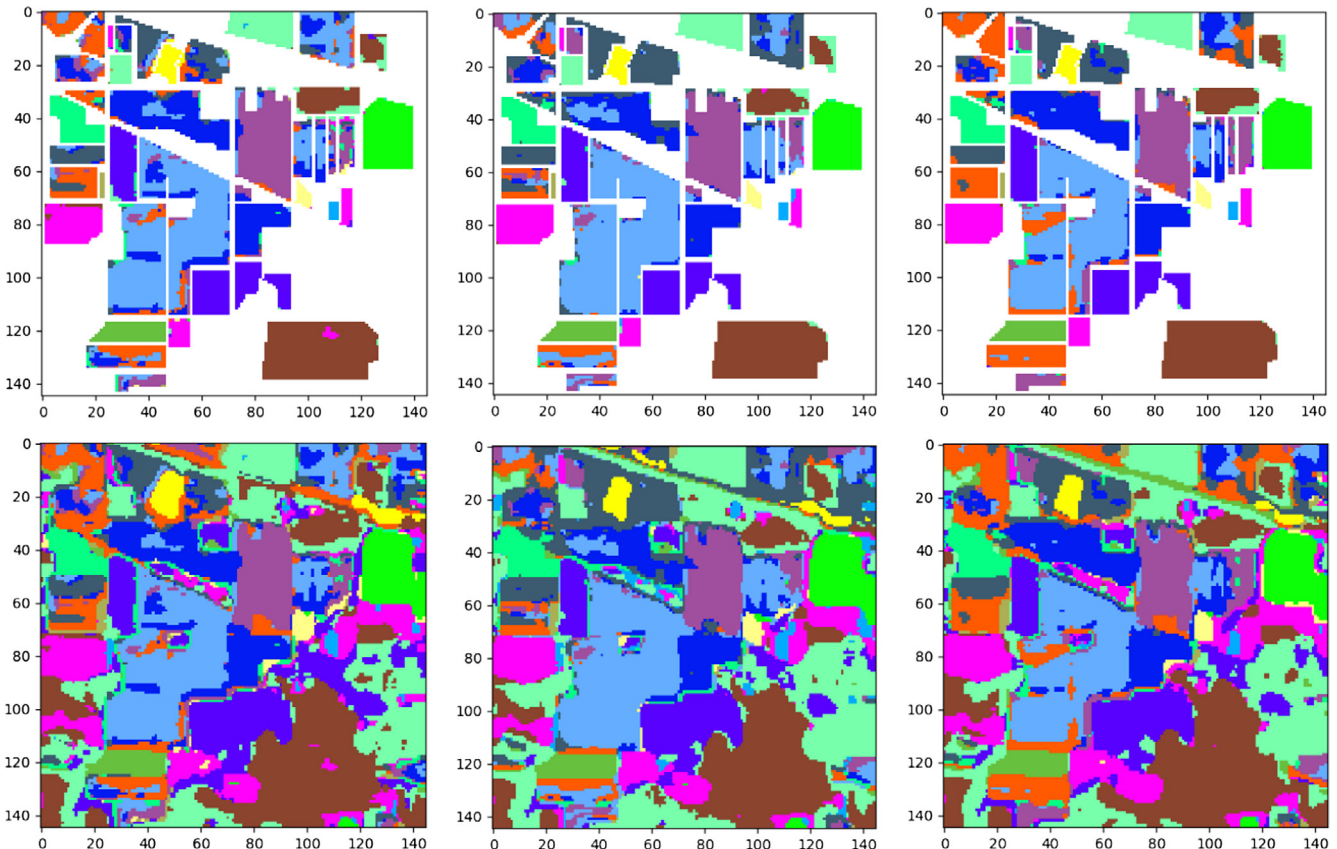


**Fig. 13.** Classification results for Indian Pines image with  $d = 9$  and 50 (left), 100 (center) and 200 (right) samples per class. The upper row displays the classification result without the background, and the lower row displays the classification result with the background.

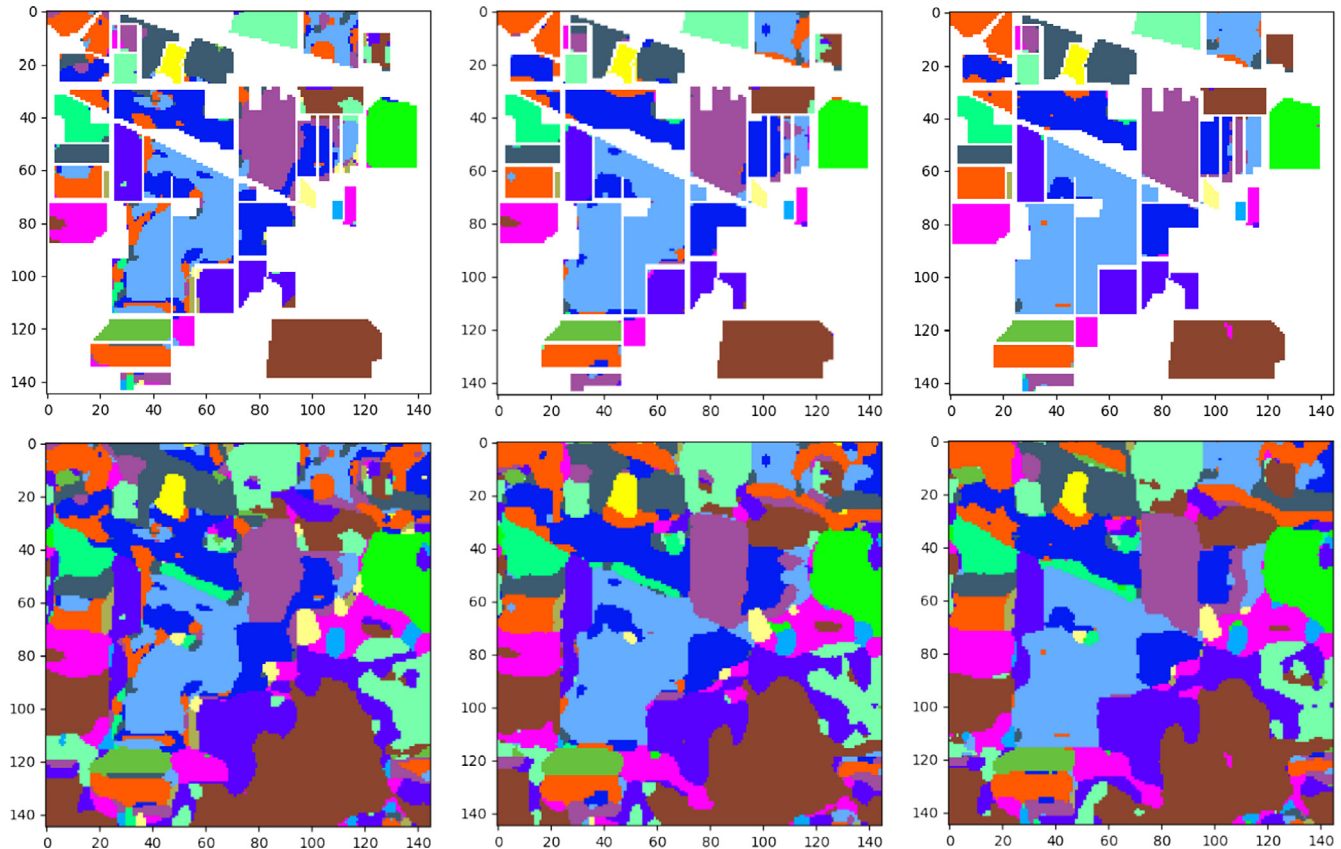


**Fig. 14.** Classification results for Indian Pines image with  $d = 19$  and  $50$  (left),  $100$  (center) and  $200$  (right) samples per class. The upper row displays the classification result without the background, and the lower row displays the classification result with the background.

result is achieved. After we get 75% sampling of each class, we set a maximum number of samples per class (as a threshold), for example 50, 100 or 200 samples per class. For those classes with many samples, we simply cut the samples until reaching the threshold. However, for those classes that have very few samples and do not reach the threshold, only those available pixels are taken. In Table 1 we can observe the real number of samples that we are using in each experiment when we refer to “50 samples per class”, “100 samples per class” or “200 samples per class”. Except for those classes that do not reach the proposed threshold (and that use 75% complete), the rest of classes work with 15–25% of their samples. In Table 2 we can see that the same solution is adopted for the University of Pavia data. In both cases, the proposed method uses less samples than (Chen et al., 2016) with the exception of Indian Pines with 200 samples per class.

#### 4.3. Hyperparameter tuning

The first step to carry out the experiments has been to adjust the configuration parameters of the convolutional network to get the best possible classification accuracy in the considered hyperspectral datasets, through cross-validation.

For the Indian Pines dataset, the CNN configuration parameters have been adjusted according to Table 3. As we can see in the convolution layers, the noise of some of the Indian Pines image bands is mitigated by a first expansion of depth, and the overfitting problem is solved by adding dropout in the first and second convolution layers and in the first fully connected layer.<sup>13</sup> The third convolution

layer refines the  $c_2$ 's feature maps with the objective of obtaining a better classification.

For the University of Pavia dataset, the CNN configuration parameters have been adjusted according to Table 3. Also, we improved the quality of the spectral information by extending the depth of the feature maps in the first convolution. In this case, the overfitting problem is worse than in the Indian Pines scene (mainly due to the greater number of parameters to be learned), so we increased the value of the dropout in the first and second convolution layers. Again, the third convolution layer refines the  $c_2$ 's feature maps, with the objective of obtaining a better classification.

#### 4.4. Performance evaluation

To test the proposed CNN for hyperspectral image classification with the configurations described in Section 4.3, several experiments have been conducted, first with the Indian Pines hyperspectral dataset and, second, with the University of Pavia hyperspectral dataset. At this point, we emphasize that data pre-processing plays a very important role in this kind of deep learning algorithms. In practice, many classification methods work better after a data normalization procedure. In this case hyperspectral datasets have been scaled between in the range  $[-0.5, 0.5]$  and a band-mean normalized procedure has been performed. This means that each of the spectral channels in the image have been normalized by subtracting the mean.

**Testing parameter  $d$ :** We tested different sizes of parameter  $d$ , using a fixed number of 100 samples per class. For the Indian Pines data, we have considered three patch sizes:  $d = 9$ ,  $d = 19$  and  $d = 29$ . In Fig. 7 we illustrate the effect of using different patch sizes over a random pixel in the Indian Pines dataset. As we add

<sup>13</sup> After the first experiment, we realized that these values were insufficient and the network was fine-tuned again. A 10% dropout was added to the third convolution layer and a 30% dropout was added to the first fully-connected layer to avoid overfitting.

pixels to the neighborhood, the spatial information around the considered pixel is more clear, especially when it comes to edge pixels. However, a patch too large can detract from the target pixel. As for the spectral signature, adding more neighbors to the target pixel also makes the signature as a whole more defined.

For the Pavia University data, we have tested other patch sizes:  $d = 15$ ,  $d = 21$  and  $d = 27$ . The difference is motivated by our pre-assessment of the size of relevant features in the image. We also provide in Fig. 8 an illustrative example of how the size of patches impacts the overall performance in the University of Pavia data set. In this case, the scene presents many object borders in the leftmost part. By adding more spatial information we can better identify the

pixels belonging to such edges. However, given the reduced number of classes, if we add too many spectral signatures we can make the patches slightly homogeneous.

For each  $d$ , we divided the original hyperspectral image into pieces (mirroring the borders of the image, if necessary) and grouping the patches into training samples and test samples. To split the patches, we followed the steps described in Section 4.2.1. Each execution of this experiment has been repeated 5 times.

Table 4 reports the obtained results. We can observe that, for the Indian Pines image,  $d = 29$  achieves the best result, reaching an overall accuracy of 95.53% with a smaller error in fewer iterations (with only 400 iterations,  $d = 29$  has already reached a

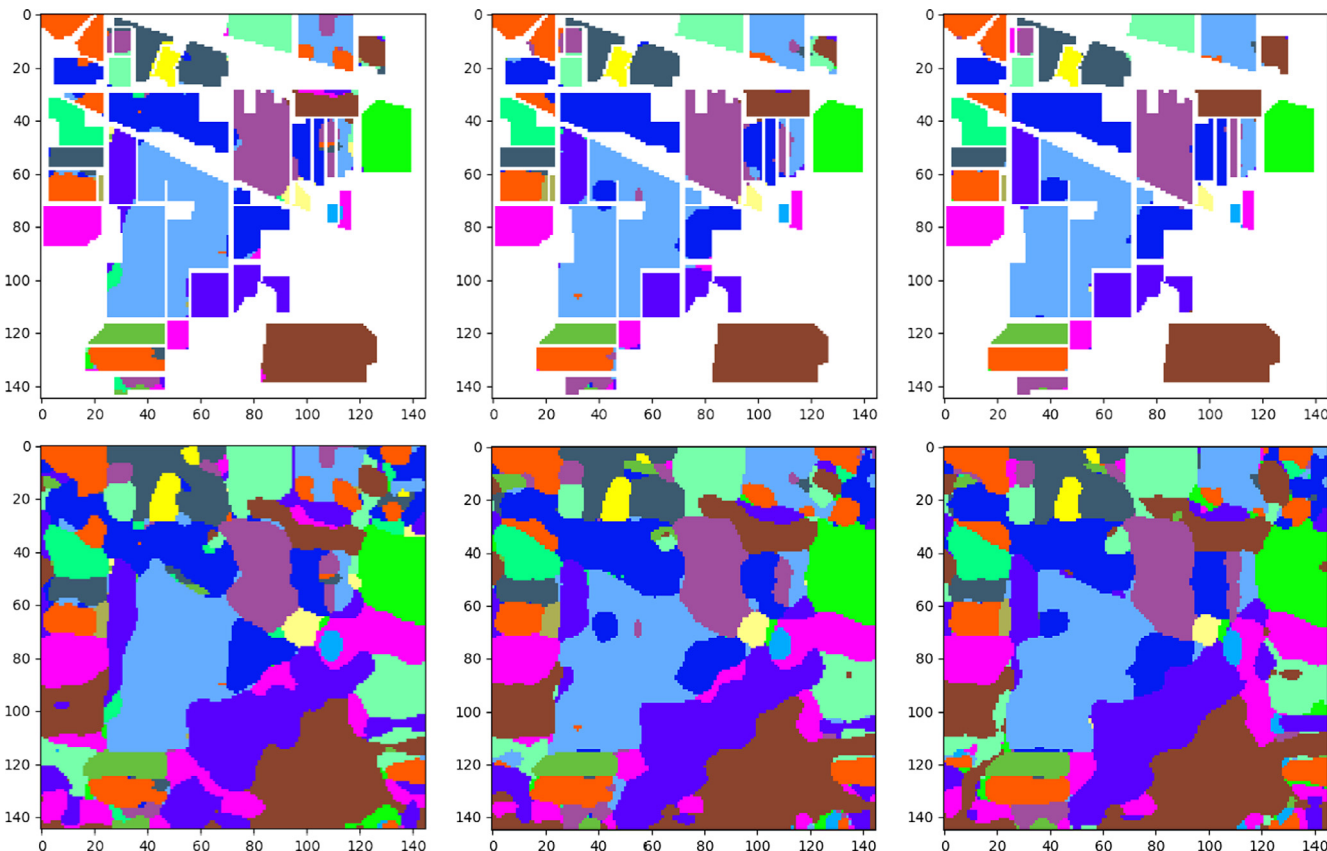


**Fig. 15.** Classification results for Indian Pines image with  $d = 29$  and 50 (left), 100 (center) and 200 (right) samples per class. The upper row displays the classification result without the background, and the lower row displays the classification result with the background.

**Table 6**

Obtained classification accuracies (with patch sizes of  $d = 15$ ,  $d = 21$  and  $d = 27$ ) for the University of Pavia hyperspectral dataset. We used 1500 iterations and repeated the experiment 5 times.

Neural networks	CNN $d = 15$			CNN $d = 21$			CNN $d = 27$		
	Samples per class	50	100	200	50	100	200	50	100
Asphalt	79.86 (4.46)	90.58 (0.74)	92.81 (0.72)	86.41 (0.47)	91.30 (1.81)	95.31 (0.97)	82.66 (1.18)	92.07 (1.05)	96.31 (0.19)
Meadows	88.97 (1.65)	94.20 (1.94)	97.20 (0.95)	89.44 (4.85)	93.39 (1.52)	98.16 (0.12)	90.39 (3.03)	93.56 (1.76)	97.54 (0.39)
Gravel	83.52 (1.92)	92.28 (2.12)	96.97 (0.90)	85.31 (4.51)	92.01 (3.55)	97.92 (0.59)	88.74 (0.90)	93.66 (1.16)	96.84 (0.29)
Trees	96.31 (1.02)	97.45 (1.34)	98.62 (0.43)	94.36 (0.49)	96.87 (0.74)	98.74 (0.18)	90.88 (1.35)	94.51 (2.12)	97.58 (0.41)
Painted metal sheets	99.83 (0.09)	99.93 (0.11)	100.00 (0.00)	99.38 (0.13)	99.88 (0.09)	100.00 (0.00)	99.31 (0.21)	99.53 (0.37)	99.65 (0.15)
Bare Soil	90.72 (1.47)	95.18 (0.93)	98.57 (0.74)	93.54 (2.45)	98.50 (1.20)	99.57 (0.31)	88.73 (2.00)	97.67 (0.88)	99.33 (0.25)
Bitumen	91.88 (1.61)	92.38 (1.22)	97.27 (0.96)	91.00 (0.57)	96.19 (1.50)	99.75 (0.09)	92.73 (1.25)	95.16 (1.29)	98.90 (1.14)
Self-Blocking Bricks	82.91 (5.26)	92.07 (1.49)	96.17 (1.70)	89.77 (2.62)	94.41 (0.93)	98.20 (0.21)	91.74 (1.49)	94.88 (1.43)	98.89 (0.47)
Shadows	99.65 (0.22)	99.54 (0.51)	99.86 (0.13)	99.65 (0.10)	99.75 (0.13)	99.82 (0.18)	97.40 (1.87)	98.91 (0.88)	99.58 (0.09)
Overall Accuracy	88.17 (0.31)	93.95 (0.74)	96.83 (0.19)	90.22 (1.78)	94.37 (1.10)	98.06 (0.13)	89.58 (1.95)	94.35 (1.05)	97.80 (0.22)
Average Accuracy	90.40 (0.38)	94.85 (0.41)	97.50 (0.14)	92.10 (0.63)	95.81 (0.82)	98.61 (0.09)	91.40 (1.26)	95.55 (0.68)	98.29 (0.25)
Kappa	84.63 (0.36)	92.07 (0.94)	95.83 (0.24)	87.28 (2.21)	92.63 (1.42)	97.44 (0.18)	86.37 (2.50)	92.61 (1.35)	97.09 (0.29)
Run time	43.02 (0.01)	42.78 (0.01)	42.83 (0.01)	74.30 (0.01)	74.17 (0.01)	74.09 (0.01)	132.77 (0.02)	132.48 (0.02)	132.68 (0.02)

minimum error, while for  $d = 19$  it needs about 1000 iterations to reach the same error and  $d = 9$  is not able to reduce its error in 1500 iterations, see Fig. 9). However, the time required for each step when  $d = 29$  is adopted is greater than with  $d = 19$  or  $d = 9$ : each step of  $d = 29$  is 0.08 s slower than the steps of  $d = 19$  and 0.14 s slower than the steps of  $d = 9$  (see Fig. 10). In terms of the accuracy/time ratio, the best option is  $d = 19$ , although the best accuracy is achieved by using  $d = 29$  (but its execution time is larger).

On the other hand, the results obtained for the University of Pavia dataset are also shown in Table 4. In this case, the patch with size  $d = 21$  achieves the best accuracy results: 95.08% in 74.66 s, reaching 1.06 percentage more than  $d = 15$  and 0.95 percentage

more than  $d = 27$ . As for the number of iterations, in Fig. 11 we can see that  $d = 27$  needs less iterations to reach an acceptable error (between 700–800 iterations) while  $d = 21$  needs around 1000–1100 iterations, which is very similar to  $d = 15$  that also needs around 1000–1100 iterations to reach a low error. On the other hand, the time per iteration for each patch size is different, being the fastest  $d = 15$  (2.15 times faster than  $d = 21$  and 3.79 times faster than  $d = 27$ ) and the slowest  $d = 27$  (around 1.76 times slower than  $d = 21$ ), see Fig. 12. With this information at hand, we can conclude that the best patch size is  $d = 21$ , as it reaches the best result in a fairly reasonable time.

**Testing the number of samples per class:** At this point, we tested the accuracy achieved for different patch sizes

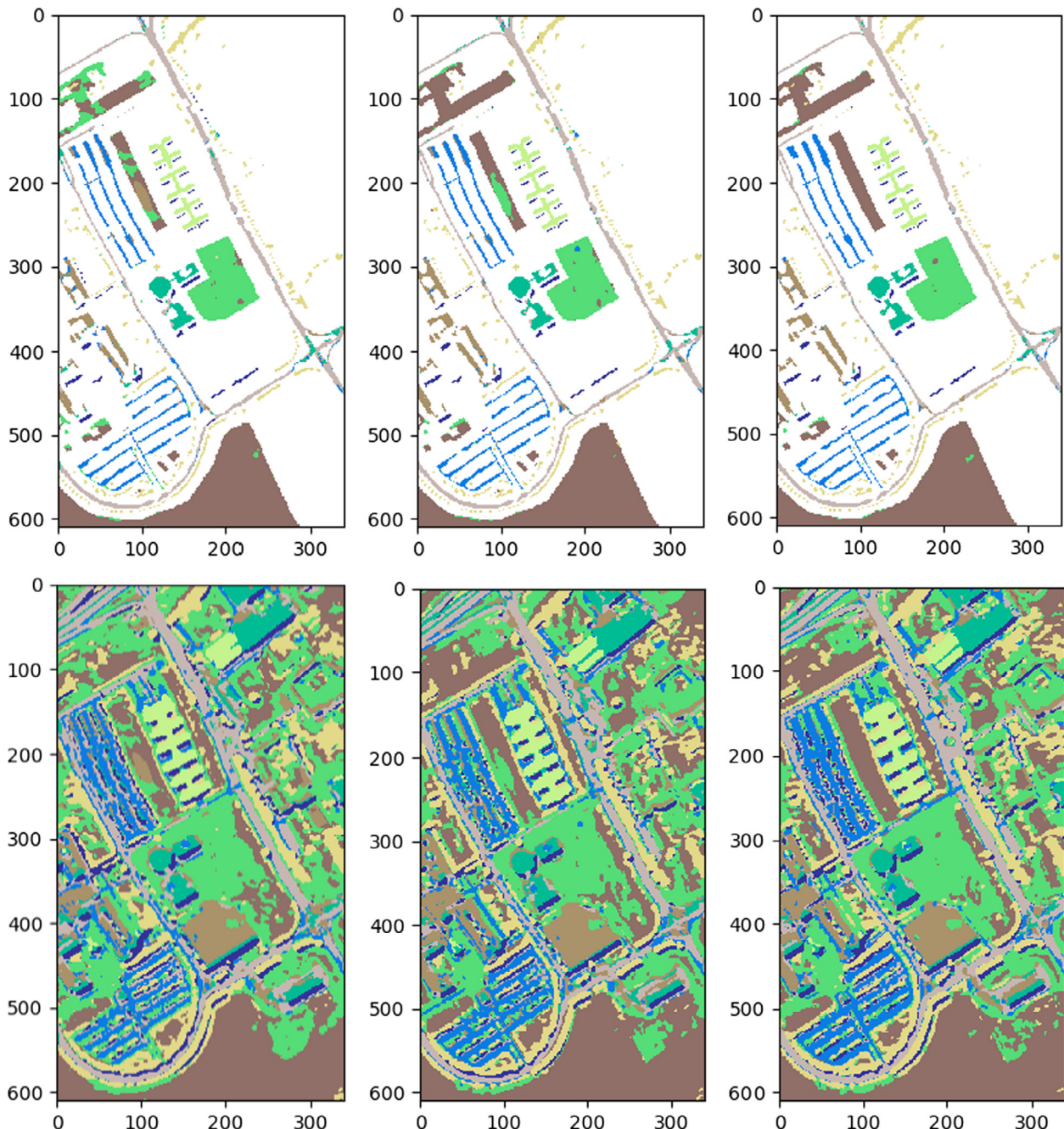


**Fig. 16.** Classification results for the University of Pavia data set with  $d = 15$  and 50 (left), 100 (center) and 200 (right) samples per class. The upper row displays the classification result without the background, and the lower row displays the classification result with the background.

( $d = 9, d = 19$  and  $d = 29$  for Indian Pines and  $d = 15, d = 21$  and  $d = 27$  for Pavia) with different amounts of training data, in particular with 50, 100 and 200 samples per class.

The results obtained for the Indian Pines dataset are shown in Table 5 (with standard deviation). In this case, for each experiment the parameters of the CNN have been fine tuned, in order to achieve the best possible accuracy. As we can observe in Figs. 9 and 10, the configuration of the CNN in Table 3 for Indian Pines presents a marked overfitting problem (that the standard deviation also seems to indicate). As a result, the dropout percentages have been modified for the Indian Pines experiment, specifically we add a 10% dropout in the third convolution layer and raise the

dropout from 10% to 30% on the first fully-connected layer. Also, for this experiment we have increased the number of iterations from 1500 to 2500. Thanks to the overfitting reduction, the network is able to converge much faster, drastically reducing the initial execution times (i.e., being 1.32 times faster with  $d = 9$ , 1.57 times faster with  $d = 19$  and 1.66 times faster with  $d = 29$  with 100 samples per class). In addition, stability has been improved by reducing the standard deviation of each run to 0.01. In Table 5 we can observe that the results with  $d = 9, d = 19$  and  $d = 29$  increase (in terms of accuracy) as more training samples per class are included, reaching the maximum values with 200 samples per class. Again,  $d = 29$  reaches the best accuracy results with 200

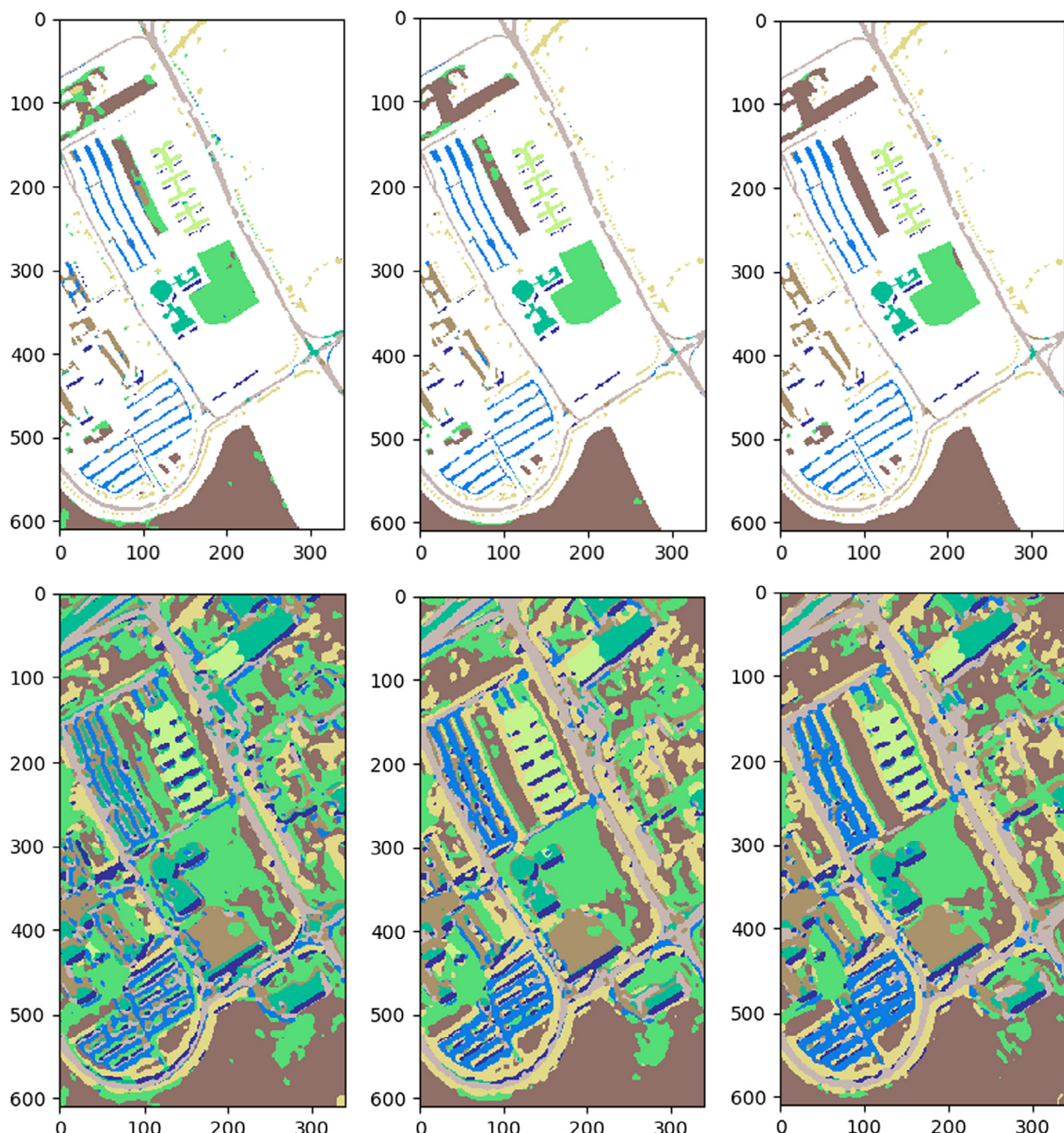


**Fig. 17.** Classification results for the University of Pavia data set with  $d = 21$  and 50 (left), 100 (center) and 200 (right) samples per class. The upper row displays the classification result without the background, and the lower row displays the classification result with the background.

samples per class, although the results obtained with a patch size of  $d = 19$  are quite similar to those found using  $d = 29$ , just one or two percentage points below.

In Figs. 13–15 we report the classification maps obtained in each experiment, without the mirroring of the borders. First, in Fig. 13 we can see the classified image without background (the first three images) and with background (the last three), obtained with a patch size of  $d = 9$  and 50, 100 and 200 samples per class. When the background is removed, we can see how the pixels of each class are mixed, in particular near the edges. Also, with background the results are poorly defined, although these are improved by adding more training samples in each class.

Secondly, in Fig. 14 we can see the classified images (with and without background) obtained with a patch size of  $d = 19$  and 50,

100 and 200 samples per class. With better results than with  $d = 9$ , the borders between the classes are better defined in this case, also in the classification with background. The best result is achieved with 200 samples per class.

Finally, in Fig. 15 we can observe the obtained classified images with a patch size of  $d = 29$ . First we report the classification images without background and below them, we show the corresponding ones with background. With only ground-truth pixels, the first three images show better defined classes than the previously displayed ones with  $d = 9$  and  $d = 19$ , being the classification map obtained with 200 samples per class the most similar to the original ground-truth image. Even in the classification with background, classes appear better defined since the borders between them are more regular.

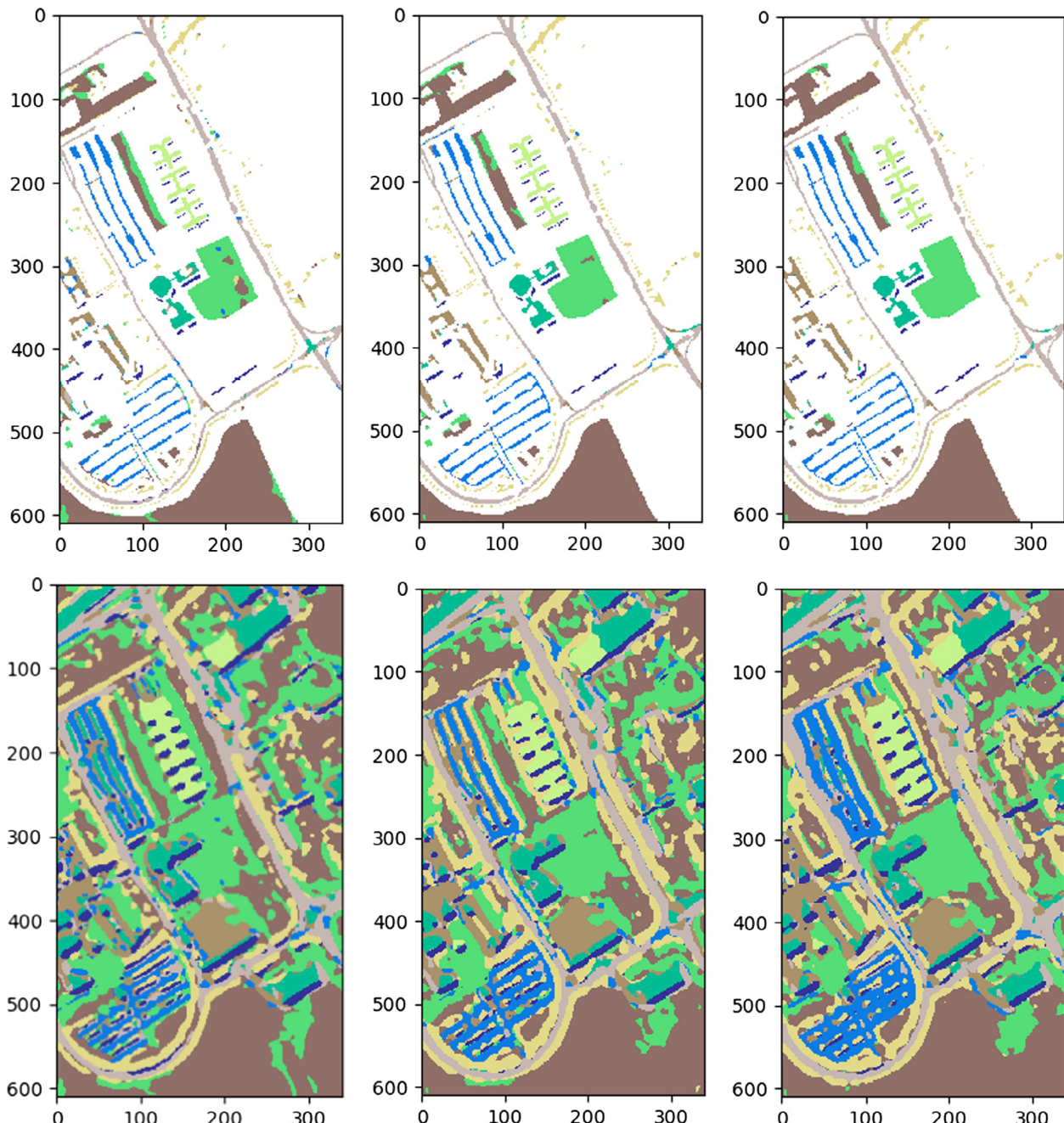


**Fig. 18.** Classification results for the University of Pavia data set with  $d = 27$  and 50 (left), 100 (center) and 200 (right) samples per class. The upper row displays the classification result without the background, and the lower row displays the classification result with the background.

On the other hand, the results for the University of Pavia dataset are shown in Table 6. For each patch size, we can observe that the accuracy improves as the number of samples per class increases, reaching the best accuracy results with 200 samples per class. If we look for the most suitable patch size, we can say that  $d = 21$  with 200 samples per class can be considered the best, with similar and balanced accuracy data. This is because, after adding more neighbors to the pixel, the data become more homogeneous.

In Figs. 16–18 we report the classification maps obtained for the University of Pavia dataset obtained in each experiment. The first one, Fig. 16 shows the Pavia classification results with a patch size of  $d = 15$ . Here, the accuracy becomes better when the number of samples per class is increased, although there are many mixed pixels in the three cases, especially when the background is added to the classification. We can observe a poor result on top of the meadows class, and the ones adjacent to the light green bare soil at the lowest part of the image.

Fig. 16 shows the Pavia classification results with a patch size of  $d = 21$ , which results in better results than  $d = 15$ . Pixels appear better defined, also with background. As expected, the best classification map is obtained with the maximum number of samples per class, i.e. 200, where we can see how the worst ranked pixels in the experiment with  $d = 15$  are now better classified, e.g. the pixels at the top of the meadows class and the bare soil pixels.

Finally, in Fig. 18 the classification results with patch size  $d = 27$  are shown. As in the previous cases, the result improves as more pixels are added to the training set (with 200 samples per class resulting in the best accuracy results). Although the pixels at the top of the image are better classified, the CNN finds it more difficult to classify the pixels of the meadow class in the center of the image, and the final result is slightly worse than the one obtained with patch size of  $d = 21$ .

#### 4.5. Comparison with other algorithms

In this section we show comparisons of our proposed method with other existing methods, including a standard MLP and the 1-D, 2-D and 3-D CNNs in Chen et al. (2016). This represents an exhaustive and complete validation of our method with state-of-the-art CNNs in the hyperspectral imaging literature. Tables 7 and 8 respectively show the configurations (for both scenes) of the MLP and CNNs used in experiments for comparison purposes.

**Comparison with MLP:** For the MLP, the chosen topology is a *single layer feedforward network* (SLFN) with three layers: an input layer which receives a pixel in all its bands, a hidden layer whose number of nodes is calculated by  $(n.\text{bands} + n.\text{classes}) \cdot \frac{2}{3}$ , with a ReLU as activation function, and an output layer with the number of nodes equals as the number of classes and a *softmax* function. So, the final MLP topology for the Indian Pines hyperspectral data set is 200 – 144 – 16 and for the University of Pavia data set is 103 – 75 – 9, both with Adam optimizer (Kingma and Ba, 2014) and 0.0045 of learning rate. The proposed topologies have been

**Table 7**  
Configuration of the MLP used in experiments for comparative purposes.

Hyperspectral datasets	MLP Topologies		
	Type	Layers	
		Nº neurons	Activation Function
Indian Pines	Input	200 ( <i>nº bands</i> )	-
	Hidden	144 ( <i>optimal nº</i> )	ReLU
	Output	16 ( <i>nº classes</i> )	Softmax
University of Pavia	Input	103 ( <i>nº bands</i> )	-
	Hidden	75 ( <i>optimal nº</i> )	ReLU
	Output	9 ( <i>nº classes</i> )	Softmax
Common parameters			
Batch size	Iterations	Learning rate	Optimizer
100	5000	0.045	AdamOptimizer

**Table 8**  
Configuration of the CNNs used in experiments for comparative purposes. These are the 1-D, 2-D and 3-D CNNs configurations described in Chen et al. (2016).

1-D CNN Topologies (Chen et al., 2016)				
Hyperspectral datasets	Conv. Layers	ReLU	Pooling	
Indian Pines	1 × 5	Yes	1 × 2	
	1 × 5	Yes	1 × 2	
	1 × 4	Yes	1 × 2	
	1 × 5	Yes	1 × 2	
	1 × 4	Yes	1 × 2	
University of Pavia	1 × 8	Yes	1 × 2	
	1 × 7	Yes	1 × 2	
	1 × 8	Yes	1 × 2	
2-D CNN Topologies (Chen et al., 2016)				
Hyperspectral datasets	Conv. Layers	ReLU	Pooling	Dropout
Indian Pines	32 × 4 × 4	Yes	2 × 2	No
	64 × 5 × 5	Yes	2 × 2	50%
	128 × 4 × 4	Yes	No	50%
University of Pavia	32 × 4 × 4	Yes	2 × 2	No
	64 × 5 × 5	Yes	2 × 2	50%
	128 × 4 × 4	Yes	No	50%
3-D CNN Topologies (Chen et al., 2016)				
Hyperspectral datasets	Conv. Layers	ReLU	Pooling	Dropout
Indian Pines	128 × 4 × 4 × 32	Yes	2 × 2	No
	192 × 5 × 5 × 32	Yes	2 × 2	50%
	256 × 4 × 4 × 32	Yes	No	50%
University of Pavia	32 × 4 × 4 × 32	Yes	2 × 2	No
	64 × 5 × 5 × 32	Yes	2 × 2	50%
	128 × 4 × 4 × 32	Yes	No	50%

**Table 9**

Execution times and accuracies obtained by the MLP (with configuration: 200 – 144 – 16) for the Indian Pines scene and by the MLP (with configuration: 103 – 75 – 9) for the University of Pavia scene, using 50, 100 and 200 samples per class. This experiment has been executed using 5000 iterations.

Datasets	Samples	Time per step		Total time		Accuracy	
		average	Std. deviation	average	Std. deviation	average	Std. deviation
Indian Pines	50	0.0036	0.0002	0.1791	0.0148	74.60	1.60
	100	0.0035	0.0001	0.1757	0.0149	79.29	1.35
	200	0.0036	0.0002	0.1800	0.0148	82.56	1.23
University of Pavia	50	0.0033	0.0001	0.1672	0.0147	82.79	1.92
	100	0.0031	0.0001	0.1550	0.0149	87.16	0.93
	200	0.0031	0.0001	0.1530	0.0149	87.76	1.75

tested with three different numbers of samples per class: 50, 100 and 200, repeating each one five times. Results are shown in **Table 9**, where we show the average time and accuracy of each

execution with 5000 iterations and repeated five times. As we can see, as we add training data the accuracy increases, however the execution time remains fairly stable.

In **Table 10** we can observe in detail the results obtained for each class of the Indian Pines dataset. After 5000 iterations, we can see that the best overall accuracy result (84.60%) is obtained with the maximum number of samples per class, i.e. 200, without an overwhelming time difference. However, even with 5000 iterations, the MLP is still not able to reach 90% overall accuracy (although it reaches a 91.66% of average accuracy). If we pay attention to **Fig. 19**, we can see how the MLP needs fewer iterations to reach a low error as the number of samples per class increases in training, with a very little difference in execution times: each iteration of MLP with 200 samples per class is only 1.01 times slower than with 50 samples and 1.02 times slower than with 100 samples per class, as we can see in **Fig. 20**. Note how the optimizer in the first second quickly evolves from a very high initial error to a more reasonable value, given the cost function under which it is iterating.

Now we can compare the MLP classifier with our proposed CNN for the Indian Pines scene. We have considered two experiments: in the first one, we compared the MLP with 100 samples per class with the proposed CNN with also 100 samples per class and patch sizes of  $d = 9$ ,  $d = 19$  and  $d = 29$ . Each classifier has been executed five times with 1500 iterations. In **Fig. 21** we can observe the evolution of the error in terms of the number of iterations of the MLP and the CNN. We can conclude that our CNN needs significantly less iterations to reach a low error when it uses patches of size  $d = 29$  and  $d = 19$  (specifically, the CNN reaches an error below

**Table 10**

Classification accuracies (and standard deviation) obtained by MLP with 50, 100 and 200 samples per class for the Indian Pines hyperspectral dataset. This experiment has been executed using 5000 iterations.

Neural network	MLP		
	50	100	200
Alfalfa	98.26 (2.54)	98.70 (1.06)	97.39 (0.87)
Corn-notill	63.40 (4.60)	71.11 (3.74)	78.36 (4.46)
Corn-min	66.00 (3.58)	82.53 (2.47)	86.17 (3.31)
Corn	86.16 (2.77)	91.31 (2.08)	92.41 (2.28)
Grass/Pasture	90.52 (2.67)	91.88 (2.30)	96.31 (1.27)
Grass/Trees	93.45 (1.35)	95.64 (1.45)	97.73 (0.94)
Grass/pasture-mowed	97.14 (2.67)	97.86 (2.86)	97.86 (2.86)
Hay-windrowed	96.32 (1.47)	97.45 (0.80)	98.62 (0.54)
Oats	99.00 (2.00)	98.00 (4.00)	100.00 (0.00)
Soybeans-notill	75.12 (4.54)	83.87 (2.11)	87.00 (2.33)
Soybeans-min	62.81 (2.86)	62.42 (5.28)	68.99 (3.70)
Soybean-clean	79.39 (1.54)	84.69 (1.13)	87.86 (1.84)
Wheat	98.54 (0.31)	99.22 (0.59)	99.41 (0.37)
Woods	83.65 (4.78)	91.07 (1.55)	94.15 (2.29)
Bldg-Grass-Tree-Drives	74.46 (1.94)	82.75 (2.30)	85.03 (4.89)
Stone-steel towers	98.49 (1.10)	99.35 (0.53)	99.35 (0.53)
Overall Accuracy	75.24 (1.51)	80.34 (1.10)	84.60 (0.71)
Average Accuracy	85.17 (1.21)	89.24 (0.41)	91.66 (0.29)
Kappa	72.18 (1.51)	77.93 (1.10)	82.65 (0.71)
Runtime (sec.)	0.1791	0.1757	0.1800

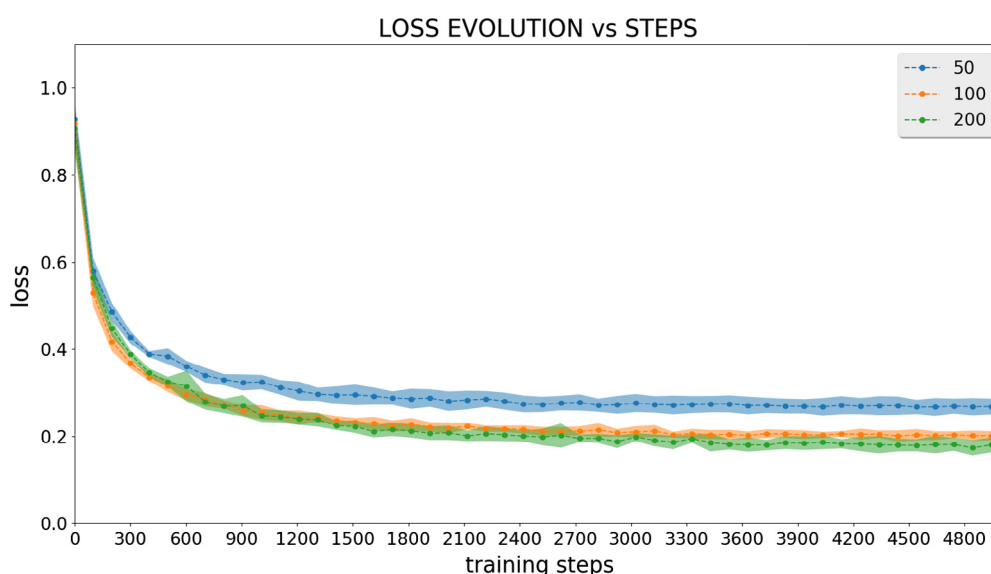


**Fig. 19.** Evolution of the validation error in terms of steps (iterations) with 50, 100 and 200 samples per class for the MLP with the Indian Pines scene. The shadow shows the standard deviation of the loss for the five executions of each patch (zoom in error interval [0, 1]). This experiment has been executed using 5000 iterations.

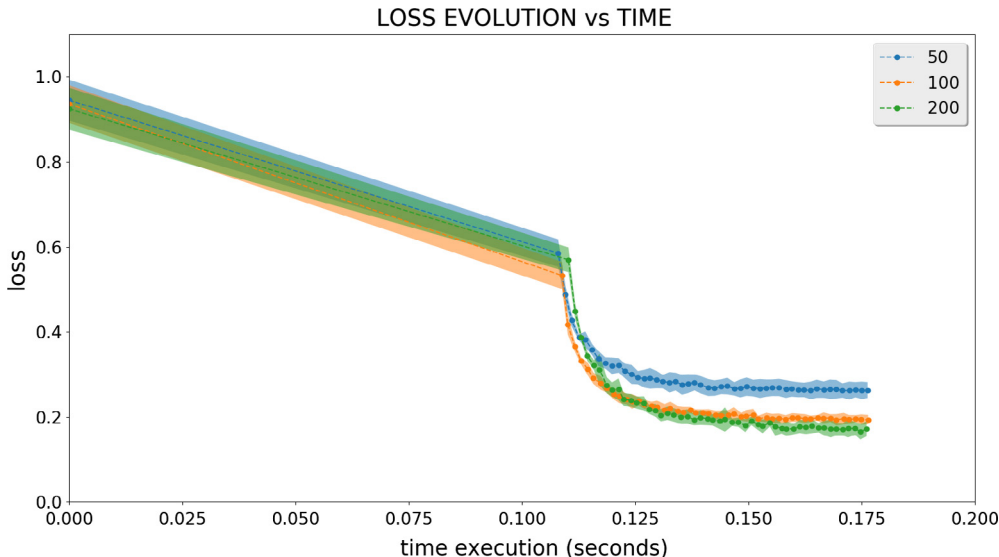


**Fig. 20.** Evolution of the validation error in terms of time (seconds) with 50, 100 and 200 samples per class for the MLP with the Indian Pines scene. The shadow shows the standard deviation of the loss for the five executions of each patch (zoom in error interval [0, 1]). This experiment has been executed using 5000 iterations.

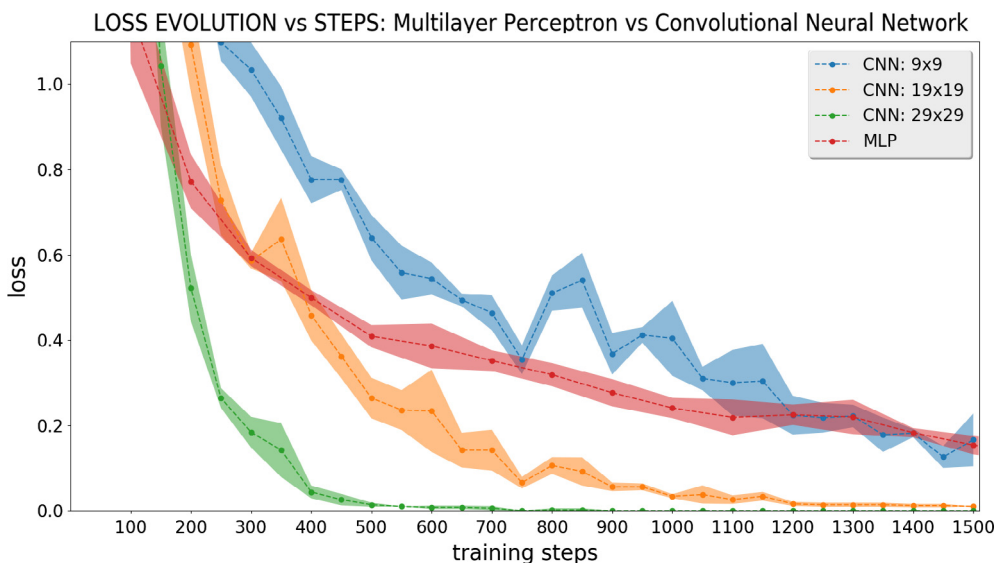


**Fig. 21.** Evolution of the validation error for the MLP and CNN (with  $d = 9$ ,  $d = 19$  and  $d = 29$ ) in terms of steps for the Indian Pines image. The shadow shows the standard deviation of the loss for each network repeated five times. Zoom in (0, 1). This experiment has been executed using 1500 iterations.

0.1 with only 300 iterations when  $d = 29$  and around 700–800 iterations when  $d = 19$ ) while the MLP barely drops from 0.2 in 1500 iterations. However, in Fig. 22 (in which we show the error evolution in terms of time in seconds) we can observe that one iteration of the CNN (with any patch size) is always slower than one iteration of the MLP.

The second comparison between the MLP and our CNN is reported in Table 12. In this case we used 200 samples per class for the MLP and CNN, and patches of size  $d = 9$ ,  $d = 19$  and  $d = 29$ . Table 12 shows that the MLP is the fastest classification method (all its executions take around 0.17–0.18 s), reaching its better average and overall accuracy values (91.66% and 84.60%, respectively) with 200 samples per class. However, these results are several points lower than the accuracies reached by the proposed CNN with patches of size  $d = 19$  and  $d = 29$ . Specifically, the MLP reaches an overall accuracy around 14 points lower than the CNN, and an average accuracy around 8 points lower than

the one achieved by the CNN for  $d = 29$ . With  $d = 19$ , the MLP reaches an overall accuracy around 11 lower than that achieved by the CNN and an average accuracy around 7 points lower than that achieved by the CNN. Only if we compare the MLP with the CNN and  $d = 9$  the MLP reaches better overall and average accuracies: around 3 points better than the overall accuracy achieved by the CNN and around 1.5 points better than the average accuracy achieved by the CNN.

The resulting classification maps obtained by the MLP are shown in Fig. 23, where the classification results without background (top row) and with background (lower row) are reported. In both cases, unlike the CNN, the MLP results are not well defined, with many pixels of different classes appearing mixed in the final classification. An increase in the number of samples per class slightly improves the classification results, without reaching the quality of the classification maps provided by the CNN in Figs. 13–15.

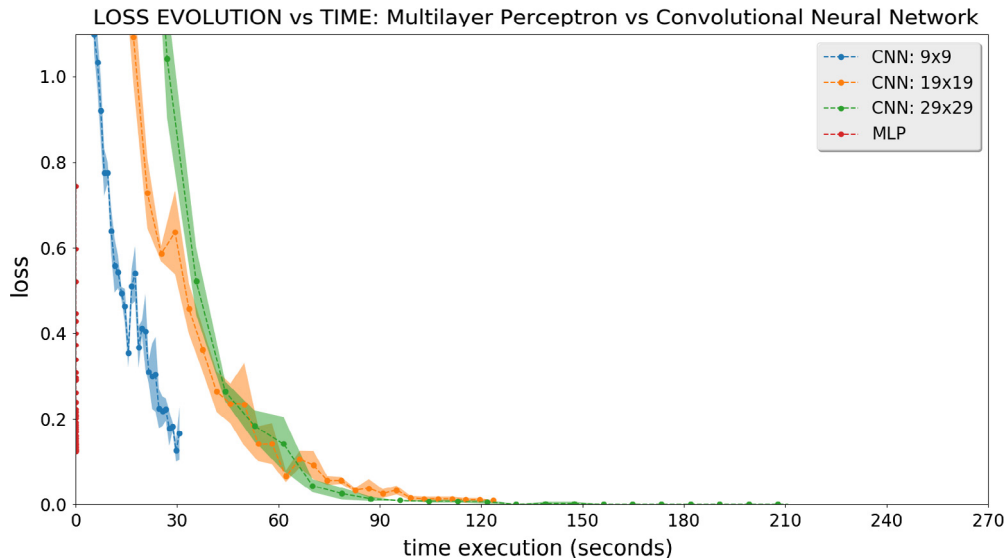


**Fig. 22.** Evolution of the validation error for the MLP and CNN (with  $d = 9$ ,  $d = 19$  and  $d = 29$ ) in terms of time (seconds) for the Indian Pines image. The shadow shows the standard deviation of the loss for each network repeated five times. Zoom in (0, 1). This experiment has been executed using 1500 iterations.

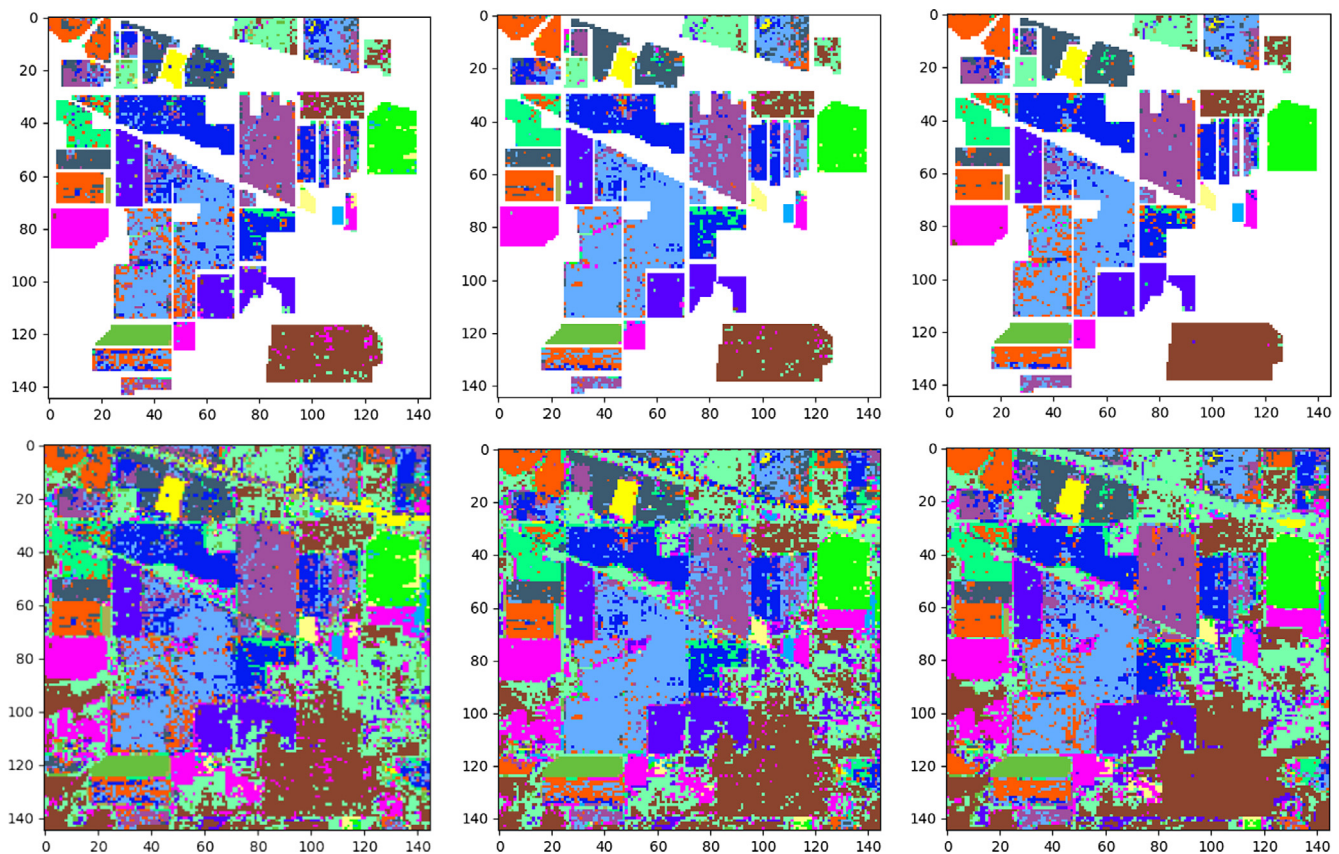


**Fig. 23.** Indian Pines classification results achieved by the MLP with 50 (left), 100 (center) and 200 (right) samples per class with 1500 iterations. The upper row displays the classification result without the background, and the lower row displays the classification result with the background.

Also, Table 9 summarizes the experiments conducted using the MLP classifier with the University of Pavia dataset for 50, 100 and 200 samples per class (all repeated five times, with 5000 iterations per execution). We can observe that the best accuracy result (87.76%) is obtained with the maximum number of samples per class, which is 200, as it was already the case with the Indian Pines

image. The execution times for 50, 100 and 200 samples per class are very similar too. However, with 5000 iterations the MLP is also unable to reach 90% accuracy. In Fig. 24 we can see how the error descends as the MLP iterates, needing less iterations as the number of samples in the training increases, with a very little difference in execution times as we can see in Fig. 25. Also, in Table 11 we can

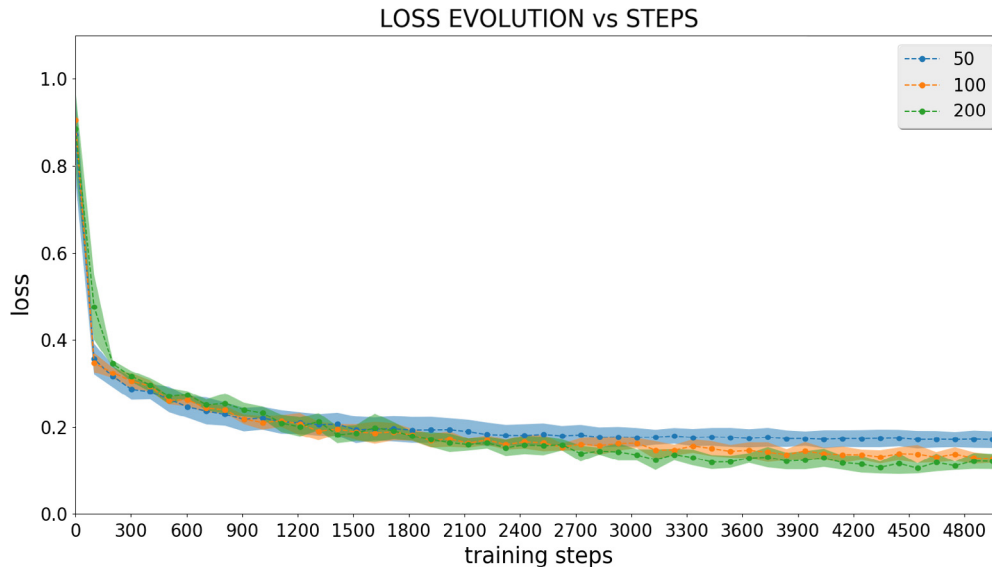


**Fig. 24.** Error evolution for the MLP in terms of steps (iterations) with 50, 100 and 200 samples per class for the University of Pavia data set. The shadow shows the standard deviation of the loss for the five executions of each patch (zoom in error interval [0, 1]).

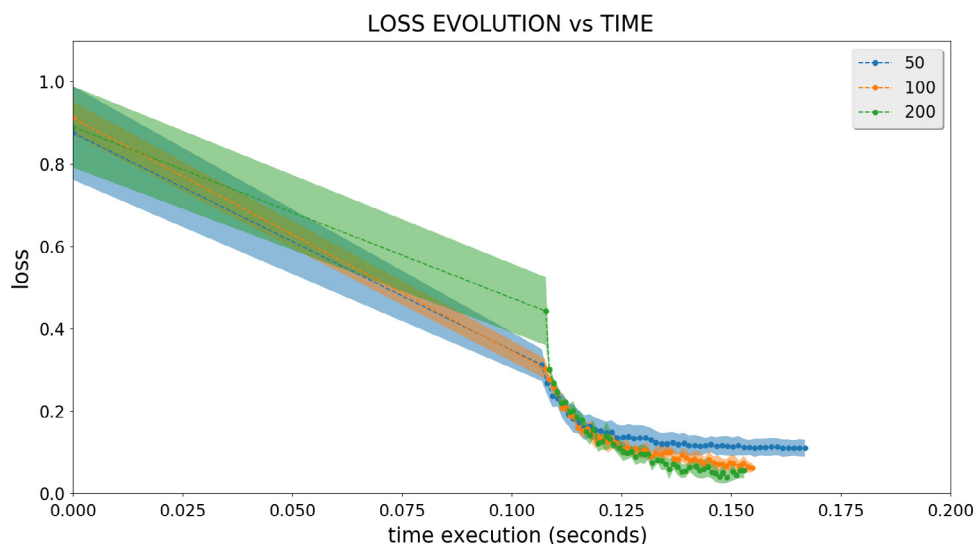


**Fig. 25.** Error evolution for the MLP in terms of time (seconds) with 50, 100 and 200 samples per class for the University of Pavia data set. The shadow shows the standard deviation of the loss for the five executions of each patch (zoom in error interval [0, 1]).

**Table 1**

Classification accuracies obtained by MLP with 50, 100 and 200 samples per class for the University of Pavia dataset.

Neural network	MLP		
Samples per class	50	100	200
Asphalt	81.29 (1.15)	83.34 (1.18)	84.92 (0.87)
Meadows	82.83 (4.46)	85.44 (2.06)	89.56 (3.75)
Gravel	84.71 (1.79)	85.98 (4.89)	94.68 (1.41)
Trees	91.64 (2.03)	94.77 (0.50)	96.48 (1.54)
Painted metal sheets	99.18 (0.16)	99.38 (0.36)	99.43 (0.30)
Bare Soil	84.87 (3.31)	88.94 (2.89)	90.75 (2.85)
Bitumen	89.35 (3.10)	92.63 (0.18)	93.76 (0.90)
Self-Blocking Bricks	79.57 (2.35)	79.50 (6.26)	63.94 (3.50)
Shadows	99.79 (0.09)	99.54 (0.36)	99.96 (0.05)
Overall Accuracy	84.37 (2.30)	86.68 (0.67)	88.20 (1.50)
Average Accuracy	88.14 (1.05)	89.95 (0.38)	90.39 (0.30)
Kappa	79.87 (2.30)	82.79 (0.67)	84.67 (1.50)
Runtime (sec.)	0.1672	0.1550	0.1530

observe the accuracy results for each class obtained after executing five times the MLP with the Pavia dataset.

Now, we can compare the results obtained by the MLP over the University of Pavia data set with the results obtained by the considered CNN architectures. In order to do so, we have performed two experiments: in the first one we execute the MLP with 100 samples per class and we choose a patch size of  $d = 15$ ,  $d = 21$  and  $d = 27$  for the CNN, and further execute it with 100 samples per class too. Each experiment has been run using 1500 iterations. In Fig. 26 we can see that the MLP needs more iterations than the CNN to reduce its associated error, without reaching in any case the error achieved by the CNN, although its iterations are faster than those of the CNN, as we can observe in Fig. 27, where it is shown that the execution time of the MLP takes less than one second.

The second experiment reports a comparison between the MLP and the proposed CNN with 200 samples per class for both

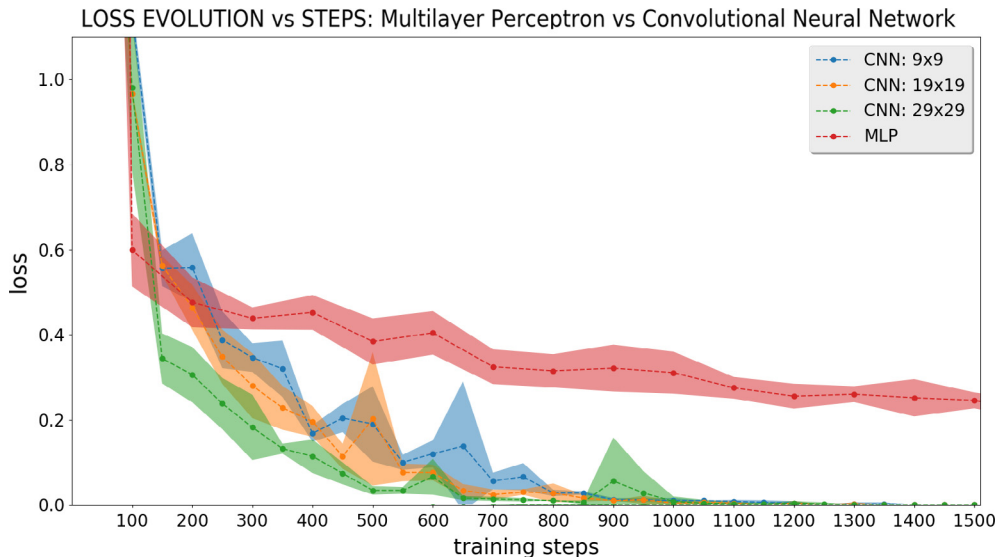


**Fig. 26.** Error evolution for the MLP and CNN (with  $d = 15$ ,  $d = 21$  and  $d = 27$ ) in terms of steps for the University of Pavia data set. The shadow shows the standard deviation of the loss for each network repeated five times. Zoom in  $(0, 1)$ .

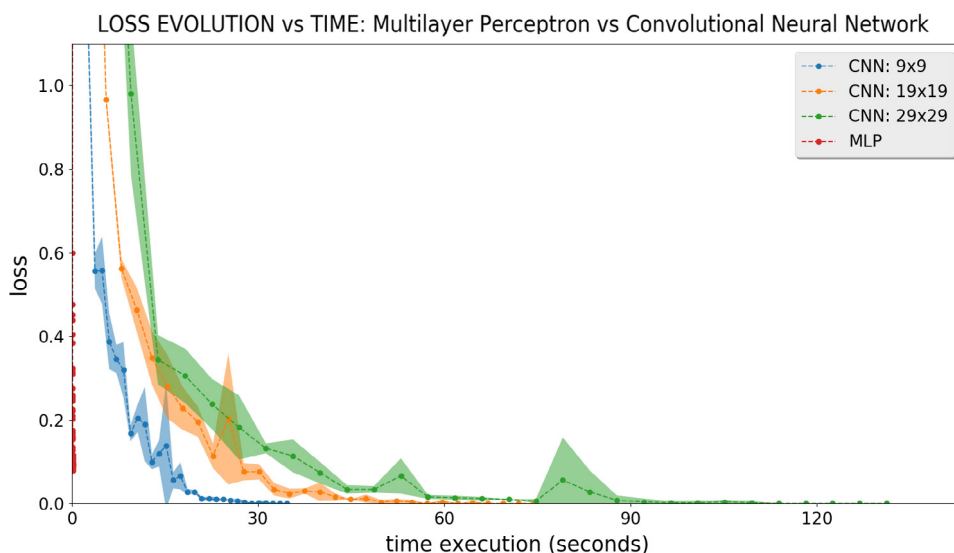


**Fig. 27.** Error evolution for the MLP and CNN (with  $d = 15$ ,  $d = 21$  and  $d = 27$ ) in terms of time (seconds) for the University of Pavia data set. The shadow shows the standard deviation of the loss for each network repeated five times. Zoom in  $(0, 1)$ .

classifiers, and patch sizes of  $d = 15$ ,  $d = 21$  and  $d = 27$  for the CNN. Table 13 shows that the MLP is the fastest classification method, even faster than the MLP with Indian Pines (all its executions take around 0.15–0.16 s), reaching its best average ad overall values (91% and 89% respectively) with 200 samples per class. But, again, the CNN reaches better accuracy values, with an average accuracy of 98% and overall accuracy of 97%, i.e. around 8–9% points better than MLP due to the inability of the latter architecture to improve its outcome.

In Fig. 28 we can observe the MLP classification maps for the University of Pavia. The top images show the classification with ground-truth pixels, whose result improves as more samples are added in the training. However the classification maps are very mixed as compared to those obtained by the CNN in Figs. 16–18. On the other hand, the bottom images show the classification with the whole background. In this case, the areas of the image are relatively well distinguished (even better when more samples per

class are added), although the number of mixed pixels is greater than in the CNN experiments with  $d = 27$ ,  $d = 21$  and  $d = 15$ .

**Comparison with other convolutional networks:** Now we compare our proposed CNN with other deep architectures, in particular with the 1-D, 2-D and 3-D CNNs described in Chen et al. (2016). In this work the authors studied the application of supervised CNNs in hyperspectral imaging feature extraction. Three deep feature extraction architectures based on the CNN were proposed to extract the spectral, spatial, and spectral-spatial features of hyperspectral imaging, respectively. To address the overfitting problem caused by the limited number of training samples, the authors implemented some regularization strategies, including L2 regularization and dropout in the training process. Also, they proposed a virtual sample enhanced method to create training samples. The main differences between our method and the one described in Chen et al. (2016) can be summarized in the following points:

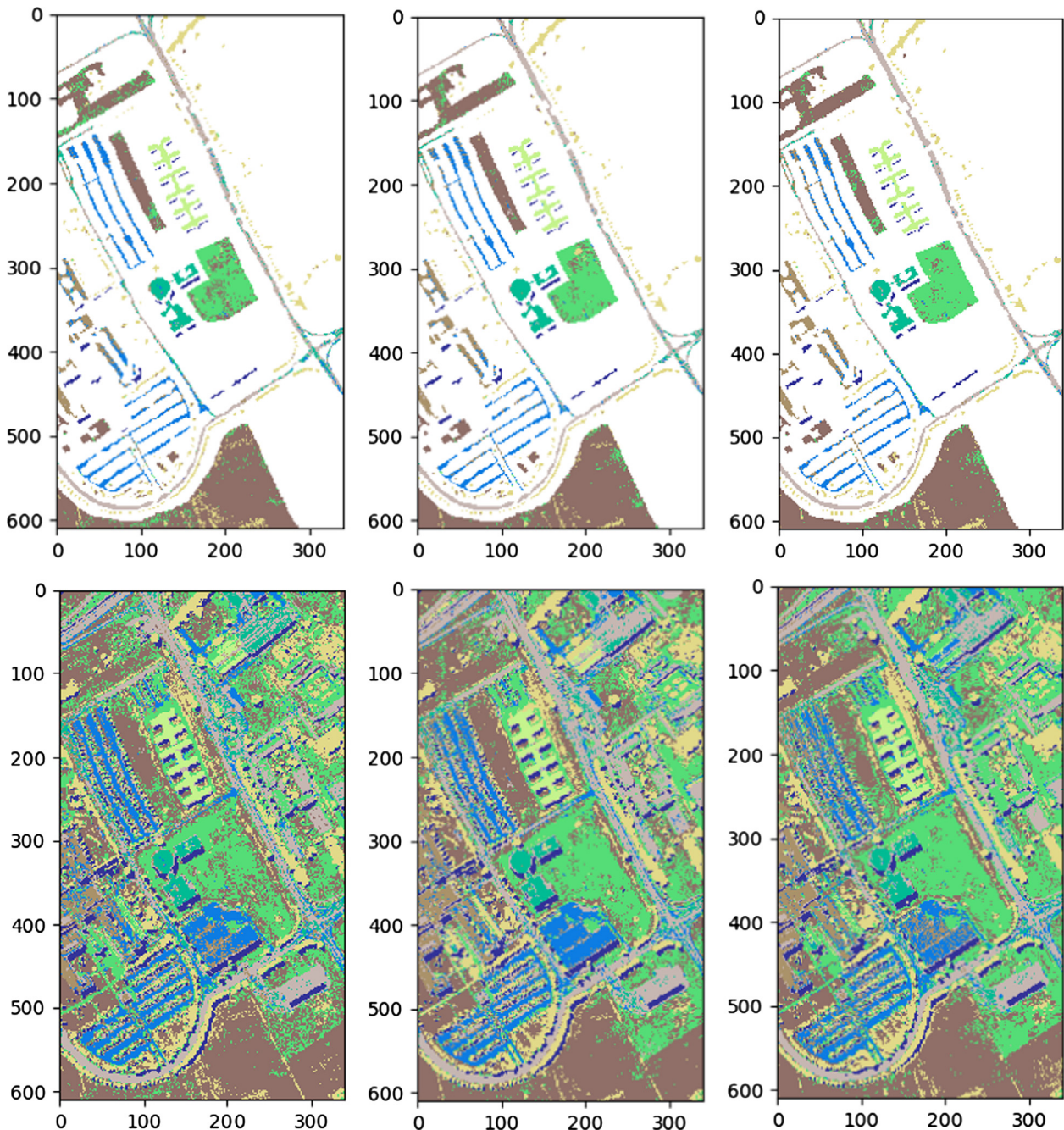


**Fig. 28.** Classification results achieved by the MLP for the University of Pavia data set with 50, 100 and 200 samples per class with 1500 iterations. The upper row displays the classification result without the background, and the lower row displays the classification result with the background.

- Regarding the configuration of the 1-D CNN, we provide a detailed description in [Table 8](#). For the Indian Pines dataset, the learning rate of the 1-D CNN is fixed to 0.005 with 700 training epochs, while for University of Pavia dataset, the learning rate is fixed to 0.001 with 600 epochs. The datasets are divided into training and testing sets. For the Indian Pines dataset, 1765 labeled pixels are chosen to create the training set, while for the University of Pavia dataset, the authors use 3930. This spectral-CNN receives a normalized pixel vector ( $1 \times 200$  if it is an Indian Pines pixel and  $1 \times 103$  if it is an University of Pavia pixel) in the range  $[-1, 1]$ . The data suffers a L2 regularization along the CNN and, at the end of the CNN procedure, the input pixel vector is converted into a feature vector that is fed to *Logistic Regression* (LR) for classification. The authors selected a mini-batch update

strategy, and the cost function is calculated on a mini-batch of inputs as  $c_o = -\frac{1}{m} \sum_{i=1}^m [x_i \log(z_i) + (1 - x_i) \log(1 - z_i)]$ , using mini-batch stochastic gradient descent as optimizer of the 1-D CNN.

- Regarding the configuration of the 2-D CNN, we provide a detailed description in [Table 8](#). This spatial-CNN receives, through a preprocessing with PCA, patches of size  $27 \times 27$  normalized in the range  $[-0.5, 0.5]$  and grouped in batches of 100. The output of the CNN is a feature vector of  $1 \times 128$  that is sent to LR for classification. As in the previous 1-D CNN, the input image is represented by some feature vectors, which capture the spatial information contained in the neighborhood region of the input pixel. Then, the learned features are fed to the LR for classification.

**Table 12**

Classification accuracies obtained by different neural networks tested using the Indian Pines dataset: (1) first column: results obtained by the MLP (trained with 200 samples per class); (2) second column: comparison between the results obtained by the 1-D CNN, 2-D CNN and 3-D CNN in Chen et al. (2016) and the results obtained by our CNN (trained with the same number of samples per class as the CNNs in Chen et al. (2016)), using different values of parameter  $d$ ; (3) third column: results obtained by our CNN (trained with 200 samples per class, using different values of parameter  $d$ ).

Neural networks	Accuracy table												
	MLP		CNNs in Chen et al., 2016 versus the proposed CNN							Proposed CNN			
	SLFN	Samples	1-D	2-D	3-D	$d = 9$	$d = 19$	$d = 29$	Samples	$d = 9$	$d = 19$	$d = 29$	Samples
Alfalfa	97.39	33	89.58	99.65	100.00	100.00	100.00	100.00	30	99.13	99.57	99.13	33
Corn-notill	78.36	200	85.68	90.64	96.34	90.57	94.06	97.17	150	80.48	94.47	98.17	200
Corn-min	86.17	200	87.36	99.11	99.49	97.69	96.43	98.17	150	96.65	98.22	98.92	200
Corn	92.41	181	93.33	100.0	100.00	99.92	100.00	100.00	100	99.66	100.00	100.00	181
Grass/Pasture	96.31	200	96.88	98.48	99.91	98.10	98.72	98.76	150	99.46	99.75	99.71	200
Grass/Trees	97.73	200	98.99	97.95	99.75	99.34	99.67	100.00	150	99.53	98.90	99.40	200
Grass/pasture-mowed	97.86	20	91.67	100.00	100.00	100.00	100.00	100.00	20	100.00	100.00	100.00	20
Hay-windrowed	98.62	200	99.49	100.00	100.00	99.58	99.92	100.00	150	99.67	99.62	100.00	200
Oats	100.00	14	100.00	100.00	100.00	100.00	100.00	100.00	15	100.00	100.00	100.00	14
Soybeans-notill	87.00	200	90.35	95.33	98.72	94.28	97.63	99.14	150	92.43	98.00	98.62	200
Soybeans-min	68.99	200	77.90	78.21	95.52	87.75	92.93	94.59	150	76.42	94.32	96.15	200
Soybean-clean	87.86	200	95.82	99.39	99.47	94.81	97.17	99.06	150	97.74	99.09	99.33	200
Wheat	99.41	143	98.59	100.00	100.00	100.00	100.00	100.00	150	99.71	100.00	99.90	143
Woods	94.15	200	98.55	97.71	99.55	98.09	97.88	99.76	150	97.71	98.85	98.96	200
Bldg-Grass-Tree-Drives	85.03	200	87.41	99.31	99.54	89.79	95.80	98.39	50	99.27	99.90	100.00	200
Stone-steel towers	99.35	75	98.06	99.22	99.34	100.00	99.57	98.92	50	100.00	100.00	100.00	75
Overall Accuracy (OA)	84.60		87.81	89.99	97.56	93.94	96.29	97.87		90.11	97.23	98.37	
Average Accuracy (AA)	91.66		93.12	97.19	99.23	96.87	98.11	99.00		96.12	98.79	99.27	
Kappa	82.65		85.30	87.95	97.02	93.12	95.78	97.57		88.81	96.85	98.15	
Runtime (sec.)	0.1800		457.8	357.0	1675.2	74.47	189.51	158.42		48.21	197.65	405.46	
Total samples		2466							1765				2466

- Finally, the configuration of the 3-D CNN is shown in Table 8. This spatial-spectral CNN receives patches of size  $27 \times 27 \times n_{bands}$  normalized in range  $[-0.5, 0.5]$  and grouped in batches of 100. In this case,  $n_{bands}$  is fixed to 32. The learning rate is fixed to 0.003 and the training epochs is set to 400. After convolutional and pooling layers, the input data is transformed and fed to LR for classification.

In Table 12 we can see a detailed comparison between the different tested neural networks using Indian Pines dataset. The first

column reports the results obtained by the MLP (trained with 200 samples per class). The second column provides a comparison between the CNNs in Chen et al. (2016) and our CNN (using the same number of samples per class as the methods in Chen et al. (2016)), with patch sizes of  $d = 9$ ,  $d = 19$  and  $d = 29$ . Finally, in the third column we also report the results obtained by our proposed CNN (trained with 200 samples per class) for comparison.

If we focus on analyzing the results provided by the different implementations of Chen et al. (2016) in the second column, we

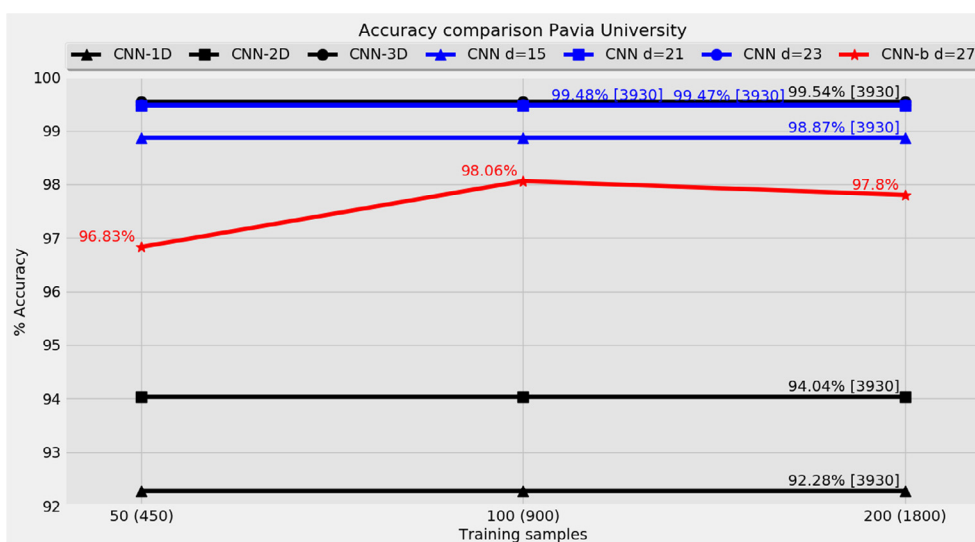


**Fig. 29.** Comparison of the overall accuracy achieved by CNN classifiers with the Indian Pines scene. The horizontal black lines show the overall accuracy results reached by the 1-D, 2-D and 3-D CNNs in Chen et al. (2016), and the horizontal blue lines show the overall accuracy results obtained by our proposed CNN, implemented with different values of  $d$  and trained with the same number of samples than the CNNs in Chen et al. (2016). The red line (marked as CNN-b in the figure) corresponds to our CNN, implemented with  $d = 29$  but trained with 50, 100 and 200 samples per class. Above each black and blue line, we report the number of used samples and the overall accuracy reached (in square brackets). For the red line, we only report the overall accuracy reached (the number of used samples for this line is defined by the x-axis). On the other hand, the y-axis shows the overall accuracies obtained in the experiments. (For interpretation of the references to color in this figure legend, the reader is referred to the web version of this article.)

can see that the one with spatial information (2-D CNN) achieves better results than the one with spectral information (1-D CNN). Also, we can see that the inclusion of the two sources of information (3-D CNN) leads to an overall improvement of the accuracy. In the same column we can observe that, when using our CNN (with the same number of samples per class as the methods in Chen et al. (2016)), the increase in the value of parameter  $d$  leads to an improvement in the obtained classification result. Also, our method is faster than all the methods reported in Chen et al. (2016) and comparable in terms of overall accuracy to the best methods reported in that work. Specifically, our proposed CNN implemented with  $d = 29$  is 2.89 times faster than the 1-D CNN, with an overall accuracy that is 10.06 percentage points better; 2.25 times faster than the 2-D CNN, with an overall accuracy 7.88 percentage points better; and 10.57 times faster than the 3-D CNN, with very similar overall accuracy. Finally, a comparison

between the results in the first and third columns of Table 12 indicate that our proposed CNN can achieve better results in terms of overall accuracy than the MLP, but the MLP is faster.

Also in Fig. 29 we provide a graphical comparison of the overall accuracy results obtained by the proposed CNN the CNNs implemented by Chen et al. (2016). The horizontal blue lines in Fig. 29 show the overall accuracy results obtained by our proposed CNN with different values of  $d$  and trained using the same number of samples than the CNNs in Chen et al. (2016). The red line corresponds to our CNN, implemented with  $d = 29$  but trained with 50, 100 and 200 samples per class. As we can see, the proposed CNN can reach better overall accuracies than the compared 1-D and 2-D CNNs. For the 3-D CNN, the results can be comparable in terms of overall accuracy. However, since our architecture is optimized and executed on a GPU, we can get better results from the viewpoint of processing time.

**Table 13**

Classification accuracies obtained by different neural networks tested using the University of Pavia dataset: (1) first column: results obtained by the MLP (trained with 200 samples per class); (2) second column: comparison between the results obtained by the 1-D CNN, 2-D CNN and 3-D CNN in Chen et al. (2016) and the results obtained by our CNN (trained with the same number of samples per class as the CNNs in Chen et al. (2016)), using different values of parameter  $d$ ; (3) third column: results obtained by our CNN (trained with 200 samples per class, using different values of parameter  $d$ ).

Neural networks	Accuracy table												
	MLP		CNNs in Chen et al., 2016 versus the proposed CNN								Proposed CNN		
	SLFN	Samples	1-D	2-D	3-D	$d = 15$	$d = 21$	$d = 23$	Samples	$d = 15$	$d = 21$	$d = 27$	Samples
Painted metal sheets	Asphalt	84.92	200	92.06	97.11	99.36	97.53	98.80	98.59	548	92.81	95.31	96.31
	Meadows	89.56	200	92.80	87.66	99.36	98.98	99.46	99.60	540	97.20	98.16	97.54
	Gravel	94.68	200	83.67	99.69	99.69	98.96	99.59	99.45	392	96.97	97.92	96.84
	Trees	96.48	200	93.85	98.49	99.63	99.75	99.68	99.57	542	98.62	98.74	97.58
	Bare Soil	99.43	200	98.91	100.00	99.95	99.93	99.78	99.61	256	100.00	100.00	99.65
	Bitumen	90.75	200	94.17	98.00	99.96	99.42	99.93	99.84	532	98.57	99.57	99.33
	Self-Blocking Bricks	93.76	200	92.68	99.89	100.00	98.71	99.88	100.00	375	97.27	99.75	98.90
	Shadows	63.94	200	89.09	99.70	99.65	98.58	99.53	99.67	514	96.17	98.20	98.89
Overall Accuracy (OA)	88.20		92.28	94.04	99.54	98.87	99.47	99.48			96.83	98.06	97.80
Average Accuracy (AA)	90.39		92.55	97.52	99.66	99.08	99.60	99.57			97.50	98.61	98.29
Kappa	84.67		90.37	92.43	99.41	98.51	99.30	99.32			95.83	97.44	97.09
Runtime (sec.)	0.15		994.80	607.19	2769.00	43.16	94.57	107.56			42.83	74.09	132.68
Total samples		1800							3930				1800

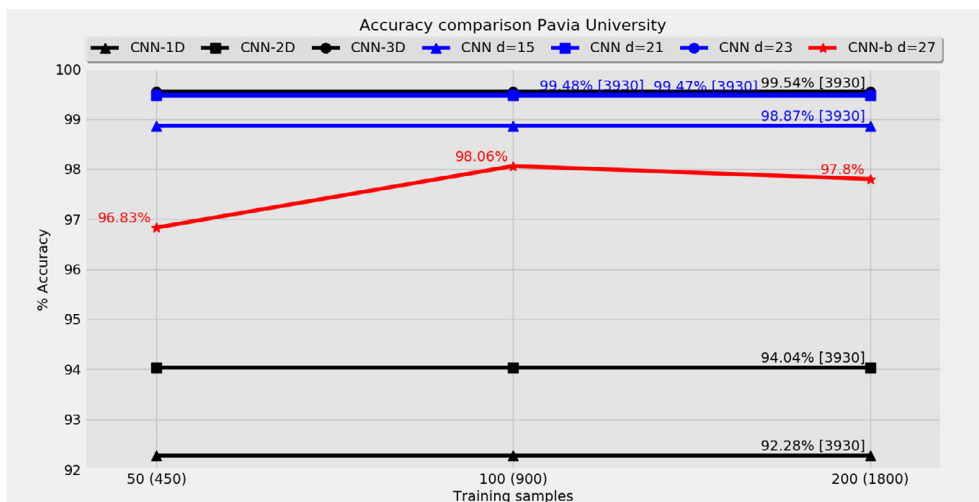


**Fig. 30.** Comparison of the overall accuracy achieved by CNN classifiers with the University of Pavia scene. The horizontal black lines show the overall accuracy results reached by the 1-D, 2-D and 3-D CNNs in Chen et al. (2016), and the horizontal blue lines show the overall accuracy results obtained by our proposed CNN, implemented with different values of  $d$  and trained with the same number of samples than the CNNs in Chen et al. (2016). The red line (marked as CNN-b in the figure) corresponds to our CNN, implemented with  $d = 29$  but trained with 50, 100 and 200 samples per class. Above each black and blue line, we report the number of used samples and the overall accuracy reached (in square brackets). For the red line, we only report the overall accuracy reached (the number of used samples for this line is defined by the x-axis). On the other hand, the y-axis shows the overall accuracies obtained in the experiments. (For interpretation of the references to color in this figure legend, the reader is referred to the web version of this article.)

In Table 13 we report a comparison between the different tested neural networks using Pavia University data set. The first column reports the results obtained by the MLP (trained with 200 samples per class). The second column provides a comparison between the CNNs in Chen et al. (2016) and our CNN (using the same number of samples per class as the methods in Chen et al. (2016)), with patch sizes of  $d = 15$ ,  $d = 21$  and  $d = 23$  (in this case, due to the number of samples per class used by Chen et al. (2016) there is not enough memory to run the CNN with  $d = 27$ ). Finally, in the third column we also report the results obtained by our proposed CNN (trained with 200 samples per class and with patch sizes of  $d = 15$ ,  $d = 21$  and  $d = 23$ ) for comparison.

Again, we can see in the second column that our method is faster than all the methods reported in Chen et al. (2016) and comparable in terms of overall accuracy to the best methods reported in that work. Specifically, our proposed CNN implemented with  $d = 23$  is 9.25 times faster than the 1-D CNN with an overall accuracy that is 7.20 percentage points better; 5.65 times faster than the 2-D CNN with an overall accuracy that is 5.44 percentage points better; and 25.74 times faster than the 3-D CNN, with very similar overall accuracy. A comparison between the results in the first and third columns of Table 13 again reveals that our proposed CNN can achieve better results in terms of overall accuracy than the MLP, but the MLP is faster.

In Fig. 30 we can graphically compare the overall accuracies obtained by our proposed CNN with those obtained by the 1-D, 2-D and 3-D CNNs reported in Chen et al. (2016). Again, the horizontal blue lines in Fig. 30 show the overall accuracy results obtained by our proposed CNN, implemented with different values of  $d$  and trained using the same number of samples than the methods in Chen et al. (2016). The red line corresponds to our CNN implemented with  $d = 27$  but trained with 50, 100 and 200 samples per class. As we can see, the proposed CNN can reach overall accuracies that are better than those achieved by the 1-D and 2-D CNNs, and comparable to those achieved by the 3-D CNN in Chen et al. (2016). However, the runtime of our implementation is considerably smaller, thanks to our GPU implementation of the network.

## 5. Conclusions and future work

In this paper, we have developed a new deep 3-D CNN architecture for spatial-spectral classification of hyperspectral data. The joint consideration of spectral information together with spatial information provides better classification results than those reached by traditional neural networks that only include spectral information. With a proper topology selection and a good election of parameters, we can obtain high classification accuracies in acceptable processing times, enforced by the fact that our CNN has been implemented efficiently using GPUs. Our detailed comparison with other 1-D, 2-D and 3-D CNNs in Chen et al. (2016) (that also include spatial and spectral information simultaneously) reveals a good compromise between the classification results obtained by our newly proposed CNN architecture and the time needed to obtain these results in the considered computing environments, which is important for practical exploitation of the proposed methodology in real applications. Our experiments specifically suggest that, with a proper and simple adaptation, the use of GPUs allows us to realize the full potential of deep learning techniques for remotely sensed hyperspectral image classification by naturally and efficiently combining the spatial and the spectral information contained in these images. This has also been verified with a classic MLP model used for comparative purposes in this work. As future work, we will conduct additional experiments with other hyperspectral scenes and

also test other high performance computing architectures for efficient implementation.

## Acknowledgement

This work has been supported by Ministerio de Educación (Resolución de 26 de diciembre de 2014 y de 19 de noviembre de 2015, de la Secretaría de Estado de Educación, Formación Profesional y Universidades, por la que se convocan ayudas para la formación de profesorado universitario, de los subprogramas de Formación y de Movilidad incluidos en el Programa Estatal de Promoción del Talento y su Empleabilidad, en el marco del Plan Estatal de Investigación Científica y Técnica y de Innovación 2013–2016). This work has also been supported by Junta de Extremadura (decreto 297/2014, ayudas para la realización de actividades de investigación y desarrollo tecnológico, de divulgación y de transferencia de conocimiento por los Grupos de Investigación de Extremadura, Ref. GR15005). Last but not least, the authors would like to take this opportunity to gratefully thank the Editors and the Anonymous Reviewers for their careful assessment of our manuscript and for their outstanding comments and suggestions, which greatly helped us to improve the technical quality and presentation of our work.

## References

- Atkinson, P.M., Tatnall, A.R.L., 1997. Introduction neural networks in remote sensing. *Int. J. Remote Sens.* 18 (4), 699–709. <https://doi.org/10.1080/014311697218700>.
- Benediktsson, J.A., Swain, P.H., 1990. Statistical Methods and Neural Network Approaches for Classification of Data from Multiple Sources (Ph.D. thesis). Purdue Univ., School of Elect. Eng. West Lafayette, IN.
- Benediktsson, J.A., Swain, P.H., Ersoy, O.K., 1993. Conjugate gradient neural networks in classification of very high dimensional remote sensing data. *Int. J. Remote Sens.* 14 (15), 2883–2903.
- Bengio, Y., 2009. Learning deep architectures for AI. *Mach. Learn.* 2 (1), 1–127.
- Bengio, Y., Lamblin, P., Popovici, D., Larochelle, H., 2007. Greedy layer-wise training of deep networks. In: Schölkopf, B., Platt, J., Hoffman, T. (Eds.), *Advances in Neural Information Processing Systems 19 (NIPS'06)*. MIT Press, pp. 153–160.
- Bishop, C.M., 1995. *Neural Networks for Pattern Recognition*. Clarendon Press <[https://books.google.es/books?id=-aAwQO\\_rXwC](https://books.google.es/books?id=-aAwQO_rXwC)>.
- Böhning, D., 1992. Multinomial logistic regression algorithm. *Ann. Inst. Stat. Math.* 44 (1), 197–200.
- Camps-Valls, G., Bruzzone, L., 2005. Kernel-based methods for hyperspectral image classification. *IEEE Trans. Geosci. Remote Sens.* 43 (6), 1351–1362.
- Chang, C.-I., 2003. *Hyperspectral Imaging: Techniques for Spectral Detection and Classification*. Springer, US.
- Chen, Y., Jiang, H., Li, C., Jia, X., Ghamisi, P., 2016. Deep feature extraction and classification of hyperspectral images based on convolutional neural networks. *IEEE Trans. Geosci. Remote Sens.* 54 (10), 6232–6251 <<http://ieeexplore.ieee.org/document/7514991/>>.
- Chen, Y., Lin, Z., Zhao, X., Wang, G., Gu, Y., 2014. Deep learning-based classification of hyperspectral data. *IEEE J. Sel. Top. Appl. Earth Observ. Remote Sens.* 7 (6), 2094–2107.
- Cheng, G., Han, J., Lu, X., 2017. Remote sensing image scene classification: benchmark and state of the art. *Proc. IEEE* (99), 1–19.
- Chien, Y., 1974. Pattern classification and scene analysis. *IEEE Trans. Autom. Control* 19 (4), 462–463.
- Cho, K., 2014. Foundations and Advances in Deep Learning (Ph.D. thesis). Aalto University.
- Deng, L., Yu, D., 2014. Deep learning: methods and applications. *Found. Trends® Signal Process.* 7 (3–4), 197–387.
- Dosovitskiy, A., Springenberg, J.T., Riedmiller, M., Brox, T., 2014. Discriminative unsupervised feature learning with convolutional neural networks. In: Ghahramani, Z., Welling, M., Cortes, C., Lawrence, N.D., Weinberger, K.Q. (Eds.), *Advances in Neural Information Processing Systems*, vol. 27. Curran Associates, Inc., pp. 766–774.
- Duchi, J., Hazan, E., Singer, Y., 2011. Adaptive subgradient methods for online learning and stochastic optimization\*. *J. Mach. Learn. Res.* 12, 2121–2159.
- Fauvel, M., Benediktsson, J.A., Chanussot, J., Sveinsson, J.R., 2008. Spectral and spatial classification of hyperspectral data using SVMs and morphological profiles. *IEEE Trans. Geosci. Remote Sens.* 46 (11), 3804–3814.
- Fisher, P., 1997. The pixel: a snare and a delusion. *Int. J. Remote Sens.* 18 (3), 679–685.
- García, V., Sánchez, J.S., Mollineda, R.A., 2011. Classification of high dimensional and imbalanced hyperspectral imagery data. In: *Proceedings Pattern Recognition*

- and Image Analysis: 5th Iberian Conference, IbPRIA 2011, Las Palmas de Gran Canaria, Spain, June 8–10, 2011. Springer, Berlin, Heidelberg, pp. 644–651.
- Ghamisi, P., Plaza, J., Chen, Y., Li, J., Plaza, A., 2017. Advanced supervised spectral classifiers for hyperspectral images: a review. *IEEE Geosci. Remote Sens. Mag.* 5 (1), 8–32.
- Glorot, X., Bengio, Y., 2010. Understanding the difficulty of training deep feedforward neural networks. In: Proceedings of the International Conference on Artificial Intelligence and Statistics (AISTATS10). Society for Artificial Intelligence and Statistics, pp. 249–256.
- Glorot, X., Bordes, A., Bengio, Y., 2011. Deep sparse rectifier neural networks. In: Gordon, Geoffrey J., Dunson, David B. (Ed.), Proceedings of the Fourteenth International Conference on Artificial Intelligence and Statistics (AISTATS-11). Journal of Machine Learning Research – Workshop and Conference Proceedings, pp. 315–323.
- Goodfellow, I.J., Pouget-Abadie, J., Mirza, M., Xu, B., Warde-Farley, D., Ozair, S., Courville, A., Bengio, Y., 2014. Generative adversarial nets. In: Ghahramani, Z., Welling, M., Cortes, C., Lawrence, N.D., Weinberger, K.Q. (Eds.), Advances in Neural Information Processing Systems, vol. 27. Curran Associates, Inc., pp. 2672–2680.
- Green, R.O., Eastwood, M.L., Sarture, C.M., Chrien, T.G., Aronsson, M., Chippendale, B. J., Faust, J.A., Pavri, B.E., Chovit, C.J., Solis, M., Olah, M.R., Williams, O., 1998. Imaging spectroscopy and the Airborne Visible/Infrared Imaging Spectrometer (AVIRIS). *Remote Sens. Environ.* 65 (3), 227–248.
- Haut, J.M., Paoletti, M., Plaza, J., Plaza, A., 2017a. Cloud implementation of the k-means algorithm for hyperspectral image analysis. *J. Supercomput.* 73 (1), 514–529. <https://doi.org/10.1007/s11227-016-1896-3>.
- Haut, J.M., Paoletti, M.E., Paz-Gallardo, A., Plaza, J., Plaza, A., 2017b. Cloud implementation of logistic regression for hyperspectral image classification. In: Vigo-Aguiar, J. (Ed.), Proceedings of the 17th International Conference on Computational and Mathematical Methods in Science and Engineering, CMMSE 2017. pp. 1063–2321.
- He, H., Garcia, E.A., 2009. Learning from imbalanced data. *IEEE Trans. Knowl. Data Eng.* 21 (9), 1263–1284.
- He, M., Li, X., Zhang, Y., Zhang, J., Wang, W., 2016. Hyperspectral image classification based on deep stacking network. In: 2016 IEEE International Geoscience and Remote Sensing Symposium (IGARSS). pp. 3286–3289.
- Hinton, G., Salakhutdinov, R., 2006. Reducing the dimensionality of data with neural networks. *Science* 313, 504–507.
- Hinton, G.E., Osindero, S., Teh, Y.-W., 2006. A fast learning algorithm for deep belief nets. *Neural Comput.* 18 (7), 1527–1554.
- Hinton, G.E., Srivastava, N., Krizhevsky, A., Sutskever, I., Salakhutdinov, R.R., 2012. Improving neural networks by preventing co-adaptation of feature detectors. CoRR. Available from: 1207.0580.
- Hochreiter, S., Schmidhuber, J., 1997. Long short-term memory. *Neural Comput.* 9 (8), 1735–1780.
- Hu, F., Xia, G.-S., Hu, J., Zhang, L., Foody, G.M., Wang, L., Thenkabail, P.S., 2015a. Transferring deep convolutional neural networks for the scene classification of high-resolution remote sensing imagery in surveying, mapping and remote sensing. *Remote Sens.* 7 (11), 14680–14707 <<http://www.mdpi.com/journal/remotesensing>>.
- Hu, W., Huang, Y., Wei, L., Zhang, F., Li, H., 2015b. Deep convolutional neural networks for hyperspectral image classification. *J. Sensors*.
- Jarrett, K., Kavukcuoglu, K., Ranzato, M.A., Lecun, Y., 2009. What is the best multi-stage architecture for object recognition? In: ICCV. IEEE, pp. 2146–2153.
- Karhunen, J., Raiko, T., Cho, K., 2015. Unsupervised Deep Learning: A Short Review.
- Khodadadzadeh, M., Li, J., Plaza, A., Ghasseman, H., Bioucas-Dias, J.M., Li, X., 2014. Spectral-spatial classification of hyperspectral data using local and global probabilities for mixed pixel characterization. *IEEE Trans. Geosci. Remote Sens.* 52 (10), 6298–6314.
- Kingma, D.P., Ba, J.L., 2014. ADAM: {A} method for stochastic optimization. CoRR. Available from: 1412.6980.
- Kunkel, B., Blechinger, F., Lutz, R., Doerrffer, R., van der Piepen, H., 1988. ROSIS (Reflective Optics System Imaging Spectrometer) – A candidate instrument for polar platform missions. In: Seelye, J., Bowyer, S. (Eds.), Optoelectronic technologies for remote sensing from space, pp. 134–141.
- Larochelle, H., Bengio, Y., 2008. Classification using discriminative restricted boltzmann machines. In: Proceedings of the 25th International Conference on Machine learning – ICML '08, pp. 536.
- LeCun, Y., Bengio, Y., Hinton, G., 2015. Deep learning. *Nature* 512, 436–444.
- LeCun, Y., Bottou, L., Bengio, Y., Haffner, P., 1998a. Gradient-based learning applied to document recognition. Proc. IEEE.
- LeCun, Y.A., Bottou, L., Orr, G.B., Müller, K.R., 1998b. Efficient backprop. In: Neural Networks: Tricks of the Trade, This Book is an Outgrowth of a 1996 NIPS Workshop. Springer-Verlag, pp. 9–50.
- Li, J., Bioucas-Dias, J.M., Plaza, A., 2010. Semisupervised hyperspectral image segmentation using multinomial logistic regression with active learning. *IEEE Trans. Geosci. Remote Sens.* 48 (11), 4085–4098.
- Li, J., Bioucas-Dias, J.M., Plaza, A., 2011. Hyperspectral image segmentation using a new Bayesian approach with active learning. *IEEE Trans. Geosci. Remote Sens.* 49 (10), 3947–3960.
- Li, M., Zang, S., Zhang, B., Li, S., Wu, C., 2014a. A review of remote sensing image classification techniques: the role of spatio-contextual information. *Eur. J. Remote Sens.* 47, 389–411.
- Li, T., Zhang, J., Zhang, Y., 2014b. Classification of hyperspectral image based on deep belief networks. In: Image Processing (ICIP), 2014 IEEE International Conference on. pp. 5132–5136.
- Li, Y., Zhang, H., Shen, Q., 2017. Spectral-spatial classification of hyperspectral imagery with 3D convolutional neural network. *Remote Sens.* 9 (1), 67.
- Licciardi, G.A., Del Frate, F., 2011. Pixel unmixing in hyperspectral data by means of neural networks. *IEEE Trans. Geosci. Remote Sens.* 49 (11), 4163–4172.
- Liu, B., Yu, X., Zhang, P., Tan, X., Yu, A., Xue, Z., 2017. A semi-supervised convolutional neural network for hyperspectral image classification. *Remote Sens. Lett.* 8 (9), 839–848. <https://doi.org/10.1080/2150704X.2017.1331053>.
- Liu, Q., Hang, R., Song, H., Zhu, F., Plaza, J., Plaza, A., 2016. Adaptive Deep Pyramid Matching for Remote Sensing Scene Classification. CoRR. Available from: 1611.03589.
- Lu, X., Zheng, X., Yuan, Y., 2017. Remote sensing scene classification by unsupervised representation learning. *IEEE Trans. Geosci. Remote Sens.* (99), 1–10.
- Ma, X., Wang, H., Wang, J., 2016. Semisupervised classification for hyperspectral image based on multi-decision labeling and deep feature learning. *ISPRS J. Photogramm. Remote Sens.* 120, 99–107.
- Melgani, F., Bruzzone, L., 2004. Classification of hyperspectral remote sensing images with support vector machines. *IEEE Trans. Geosci. Remote Sens.* 42 (8).
- Midhun, E.M., Nair, S.R., Prabhakar, N., Kumar, S., 2014. Deep model for classification of hyperspectral image using restricted Boltzmann machine. In: Proceedings of the 2014 International Conference on Interdisciplinary Advances in Applied Computing. ACM, New York, NY, USA, pp. 35:1–35:7.
- Nair, V., Hinton, G.E., 2010. Rectified linear units improve restricted Boltzmann machines. In: Fürnkranz, Johannes, Joachims, Thorsten (Eds.), Proceedings of the 27th International Conference on Machine Learning (ICML-10). Omnipress, pp. 807–814.
- Paoletti, M.E., Haut, J.M., Plaza, J., Plaza, A., 2017. Yinyang K-means clustering for hyperspectral image analysis. In: Vigo-Aguiar, J. (Ed.), Proceedings of the 17th International Conference on Computational and Mathematical Methods in Science and Engineering, Rota, pp. 1625–1636.
- Plaza, A., Benediktsson, J.A., Boardman, J.W., Brazile, J., Bruzzone, L., Camps-Valls, G., Chanussot, J., Fauvel, M., Gamba, P., Gualtieri, A., Marconcini, M., Tilton, J.C., Trianni, G., 2009. Recent advances in techniques for hyperspectral image processing. *Remote Sens. Environ.* 113 (1), S110–S122.
- Qian, N., 1999. On the momentum term in gradient descent learning algorithms. *Neural Netw.* 12 (1), 145–151.
- Rajan, S., Ghosh, J., Crawford, M.M., 2008. An active learning approach to hyperspectral data classification. *IEEE Trans. Geosci. Remote Sens.* 46 (4), 1231–1242.
- Ranzato, M.A., Poulnary, C., Chopra, S., Lecun, Y., 2006. Efficient learning of sparse representations with an energy-based model. In: Schölkopf, B., Platt, J., Hoffman, T. (Eds.), Advances in Neural Information Processing Systems, vol. 19. MIT Press, pp. 1137–1144.
- Romero, A., Gatta, C., Camps-Valls, G., 2016. Unsupervised deep feature extraction for remote sensing image classification. *IEEE Trans. Geosci. Remote Sens.* 54 (3), 1349–1362.
- Salakhutdinov, R., Hinton, G., 2009. Deep boltzmann machines. In: 12th International Conference on Artificial Intelligence and Statistics, pp. 3.
- Scholkopf, B., Smola, A.J., 2001. Learning with Kernels: Support Vector Machines, Regularization, Optimization, and Beyond. MIT Press, Cambridge, MA, USA.
- Smolensky, P., 1986. Information processing in dynamical systems: foundations of harmony theory. In: Rumelhart, David E., McClelland, J.L. (Eds.), Parallel Distributed Processing: Explorations in the Microstructure of Cognition, Foundations, vol. 1. MIT Press, pp. 194–281 (Chapter 6).
- Starck, J.-L., Elad, M., Donoho, D.L., 2005. Image decomposition via the combination of sparse representations and a variational approach. *IEEE Trans. Image Process.* 14 (10), 1570–1582.
- Tarabalka, Y., Benediktsson, J.A., Chanussot, J., 2009. Spectral-spatial classification of hyperspectral imagery based on partialitional clustering techniques. *IEEE Trans. Geosci. Remote Sens.* 47 (8), 2973–2987.
- Vetrivel, A., Gerke, M., Kerle, N., Nex, F., Vosselman, G., 2017. Disaster damage detection through synergistic use of deep learning and 3D point cloud features derived from very high resolution oblique aerial images, and multiple-kernel-learning. *ISPRS J. Photogramm. Remote Sens.*
- Wu, Q., Diao, W., Dou, F., Sun, X., Zheng, X., Fu, K., Zhao, F., 2016. Shape-based object extraction in high-resolution remote-sensing images using deep Boltzmann machine. *Int. J. Remote Sens.* 37 (24), 6012–6022.
- Wu, Z., Wang, Q., Plaza, A., Li, J., Wei, Z., 2015. Real-time implementation of the sparse multinomial logistic regression for hyperspectral image classification on GPUs. *IEEE Geosci. Remote Sens. Lett.* 12 (7), 1456–1460.
- Xu, X., Li, J., Huang, X., Dalla Mura, M., Plaza, A., 2016a. Multiple morphological component analysis based decomposition for remote sensing image classification. *IEEE Trans. Geosci. Remote Sens.* 54 (5), 3083–3102.
- Xu, X., Li, J., Plaza, A., 2016b. Fusion of hyperspectral and LiDAR data using morphological component analysis. In: 2016 IEEE International Geoscience and Remote Sensing Symposium (IGARSS), pp. 3575–3578.
- Yang, H., 1999. A back-propagation neural network for mineralogical mapping from AVIRIS data. *Int. J. Remote Sens.* 20 (1), 97–110. <https://doi.org/10.1080/014311699213622>.
- Yang, J., Zhao, Y., Chan, J.C.W., Yi, C., 2016. Hyperspectral image classification using two-channel deep convolutional neural network. In: 2016 IEEE International Geoscience and Remote Sensing Symposium (IGARSS), pp. 5079–5082.
- Yu, S., Jia, S., Xu, C., 2017. Convolutional neural networks for hyperspectral image classification. *Neurocomputing* 219, 88–98.
- Yuan, Y., Mou, L., Lu, X., 2015. Scene recognition by manifold regularized deep learning architecture. *IEEE Trans. Neural Netw. Learn. Syst.* 26 (10), 2222–2233.

- Zeiler, M.D., 2012. ADADELTA: An Adaptive Learning Rate Method. CoRR. Available from: <1212.5701>.
- Zeiler, M.D., Krishnan, D., Taylor, G.W., Fergus, R., June 2010. Deconvolutional networks. In: 2010 IEEE Computer Society Conference on Computer Vision and Pattern Recognition, pp. 2528–2535.
- Zhang, H., Li, Y., Zhang, Y., Shen, Q., 2017. Spectral-spatial classification of hyperspectral imagery using a dual-channel convolutional neural network. *Remote Sens. Lett.* 8 (5), 438–447.
- Zhang, L., Zhang, L., Du, B., 2016a. Deep learning for remote sensing data advances in machine learning for remote sensing and geosciences. *IEEE Geosci. Remote Sens. Mag.* 4 (2), 22–40 <<http://ieeexplore.ieee.org/document/7486259/>>.
- Zhang, P., Gong, M., Su, L., Liu, J., Li, Z., 2016b. Change detection based on deep feature representation and mapping transformation for multi-spatial-resolution remote sensing images. *ISPRS J. Photogramm. Remote Sens.* 116, 24–41.
- Zhao, W., Du, S., 2016a. Learning multiscale and deep representations for classifying remotely sensed imagery. *ISPRS J. Photogramm. Remote Sens.* 128, 223–239.
- Zhao, W., Du, S., 2016b. Spectral-spatial feature extraction for hyperspectral image classification: a dimension reduction and deep learning approach. *IEEE Trans. Geosci. Remote Sens.* 54 (8), 4544–4554.
- Zhou, X., Prasad, S., 2017. Active and semisupervised learning with morphological component analysis for hyperspectral image classification. *IEEE Geosci. Remote Sens. Lett.* 14 (8), 1348–1352.